

1 **A model for interpreting the deformation mechanism of reservoir landslides in the**
2 **Three Gorges Reservoir area, China**

3 Zongxing Zou¹, Huiming Tang¹, Robert E. Criss², Xinli Hu³, Chengren Xiong¹, Qiong
4 Wu³, Yi Yuan⁴

5 ¹Three Gorges Research Center for geo-hazards, China University of Geosciences, Wuhan, 430074,
6 China

7 ²Department of Earth and Planetary Sciences, Washington University, One Brookings Drive, Saint
8 Louis, United States

9 ³Faculty of Engineering, China University of Geosciences, Wuhan, 430074, China

10 ⁴Department of Land and Resources of Hubei Province, Wuhan, 430074, China

11 *Correspondence author: Huiming Tang (tanghm@cug.edu.cn)*

12

13 **Abstract.** Landslides whose slide surface is gentle near the toe and relatively steep in the middle
14 and rear part are common in the Three Gorges Reservoir area, China. The mass that overlies the
15 steep part of the slide surface is termed the “driving section” and that which overlies the gentle part
16 of the slide surface is termed the “resisting section”. A driving-resisting model is presented to
17 elucidate the deformation mechanism of reservoir landslides of this type, as exemplified by Shuping
18 landslide. More than 13 years of field observations that include rainfall, reservoir level and
19 deformation show that the displacement velocity of Shuping landslide depends strongly on the
20 reservoir level but only slightly on rainfall. Seepage modelling shows that the landslide was
21 destabilized shortly after the reservoir was first impounded to 135 m, which initiated a period of
22 steady deformation from 2003 to 2006 that was driven by buoyancy forces on the resisting section.
23 Cyclical water-level fluctuations in subsequent years also affected slope stability, with annual
24 “jumps” in displacement coinciding with drawdown periods that produce outward seepage forces. In
25 contrast, the inward seepage force that results from rising reservoir levels stabilizes the slope, as
26 indicated by decreased displacement velocity. Corrective transfer of earth mass from the driving
27 section to the resisting section successfully reduced the deformation of Shuping landslide, and is a
28 feasible treatment for huge reservoir landslides in similar geological settings.

29 **Keywords:** Three Gorges Reservoir, Reservoir landslide, Water level fluctuation, Deformation
30 mechanism, Shuping landslide

31

32 **1 Introduction**

33 Reservoir landslides attract wide attention as they can cause huge surge waves and other
34 disastrous consequences (Huang et al., 2017; Wen et al., 2017; Froude and Petley, 2018). The surge
35 wave produced by the 1963 Vajont landslide in Italy destroyed Longarone village and caused nearly
36 2,000 fatalities (Paronuzzi and Bolla, 2012). A similar surge associated with the 2003 Qianjiangping
37 landslide, which slipped shortly after the Three Gorges Reservoir (TGR) in China was first
38 impounded, capsized 22 fishing boats and took 24 lives (Xiao et al., 2007; Tang et al., 2019). To
39 ensure the safety of the reservoir, 1.5 billion US dollars have been invested to reinforce the reservoir
40 banks in TGR. However, reinforcement structures are costly and difficult to construct, and thus many
41 huge reservoir landslides have not been treated (Wang and Xu, 2013). Many remain in a state of
42 continuous deformation, such that cumulative monitored displacements of several meters are now
43 documented at the Huangtupo (Tang et al., 2015; Zou et al., 2020; Dumperth et al., 2016), Outang
44 (Yin et al., 2016), and Baishuihe (Li et al., 2010; Du et al., 2013) landslides. Additional study of the
45 deformation and failure mechanisms, and risk reduction strategies of these huge reservoir landslides
46 is of great significance.

47 Most research on the deformation or failure mechanism of reservoir landslides involves
48 numerical modelling, physical model testing, or field observation. Many numerical simulations have
49 studied how landslide geometry, material permeability, variation rate of water level and pressure
50 variation influence the stability of reservoir landslides (Rinaldi and Casagli, 1999; Lane and Griffiths,
51 2000; Liao et al., 2005; Cojean and Cai, 2011; Song et al., 2015). Both small-scale (Junfeng et al.,

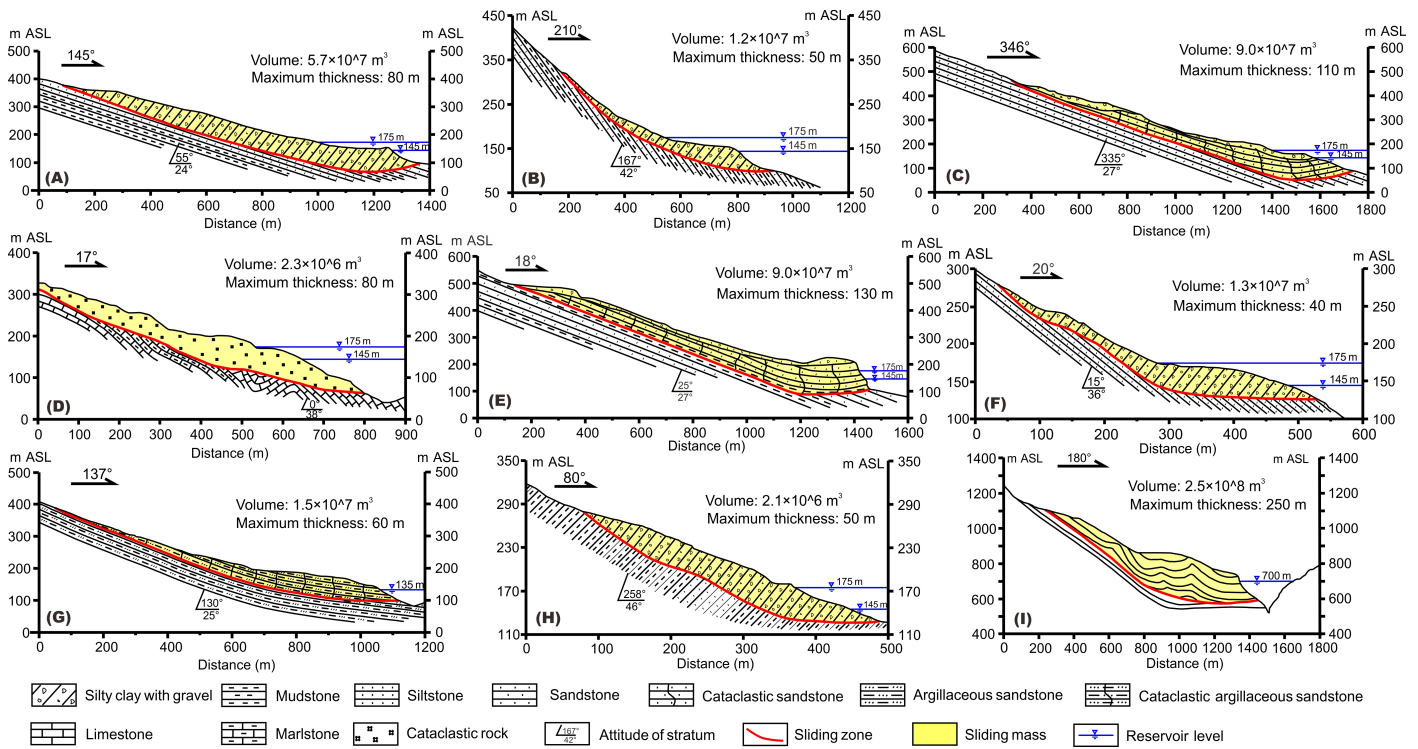
52 2004; Hu et al., 2005; Miao et al., 2018) and large-scale physical model experiments (Jia et al., 2009)
53 have been conducted to investigate the deformation features of reservoir landslides related to water
54 level change. Casagli et al. (1999) and Rinaldi et al. (2004) monitored the pore water pressure in
55 riverbanks to determine its effect on bank stability.

56 Since the impoundment of TGR, monitoring systems have been installed on or within many
57 reservoir landslides (Ren et al., 2015; Huang et al., 2017; Song et al., 2018; Wu et al., 2019), which
58 provide valuable data for the study of their deformation features. Many studies show that reservoir
59 water level variations and rainfall are the most critical factors that govern the stability and
60 **displacement** velocities of reservoir landslides in TGR (Li et al., 2010; Tang et al., 2015; Ma et al.,
61 2016; Wang et al., 2014). **These phenomena are more obvious in the landslides with lower**
62 **permeability and in the situations of rapid drawdown and heavy rainfall. In the low permeability**
63 **landslide, the groundwater is not easy to be discharged from the slope in the process of rapid**
64 **drawdown and rainfall infiltration, which results in the formation of pressure difference between**
65 **inside and outside of the landslide and reduces the stability of the landslide.** However, the effects of
66 rainfall and reservoir level are difficult to distinguish because the period of TGR drawdown is
67 managed to coincide with the rainy season. Detailed deformation studies that incorporate long-term
68 continuous monitoring data are needed to quantify how periodic water-level variations affect
69 reservoir landslides. Moreover, the evolutionary trend of these deforming landslides and feasible
70 treatments for these huge reservoir landslides are rarely studied.

71 **Many researchers have noticed that different parts of the slide mass play different role in the**

72 landslide stability. Terzaghi and Peck (1967), Sultan and Seed (1967) presented wedge method for
73 analyzing landslides consisting of an active driving wedge and resisting block. Hutchinson (1984)
74 presented an "influence-line" approach for assessing effectiveness of cuts and fills in stabilizing
75 slopes. Baum and Fleming (1991) derived expressions for the boundary between driving and
76 resisting elements of landslides for a shallow landslide. Iverson (1986), McKean and Roering (2004),
77 Guerriero et al. (2014), Prokesova et al. (2014), and Handwerger et al. (2015) have further explored
78 the influence of slip surface and landslide geometry on landslide deformation, force distribution and
79 landslide dynamics. These works provide a new perspective for the studying reservoir landslides.

80 This study presents a model combined with seepage simulations to elucidate how reservoir
81 landslides deform, using the Shuping landslide as an example. The new environmental and
82 deformation data provided here extend the observational period for this landslide to more than 13
83 years, and include results that confirm the effectiveness of a control strategy that have been
84 implemented.



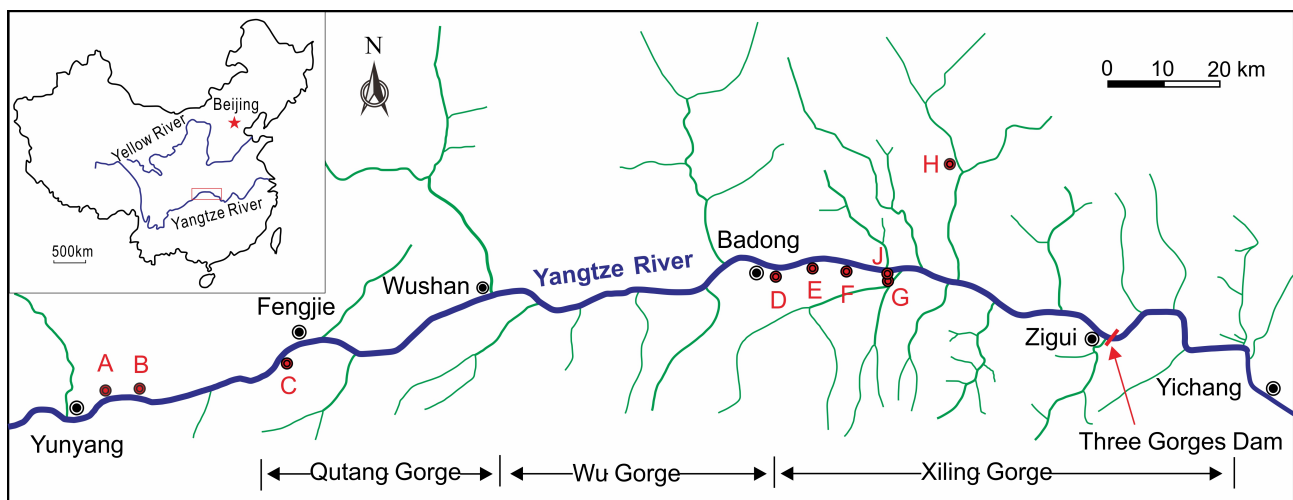
85

86 **Fig. 1** Geological profiles for typical reservoir landslides, all in the TGR except Vajont in Italy (I).
 87 (A) Jiuxianping landslide (Wang, 2013); (B) Xicheng landslide (Song, 2011); (C) Outang landslide
 88 (Yin et al., 2016); (D) No.1 riverside slump of Huangtupo landslide (Wang et al., 2014); (E)
 89 Muyubao landslide (Lu, 2012); (F) Baishuihe landslide (Lu, 2012); (G) Qiangjiangping landslide
 90 (Xiao et al., 2007); (H) Ganjuyuan landslide (Qin, 2011); (I) Vajont landslide, the world famous
 91 reservoir-induced landslide in Italy (Paronuzzi and Bolla, 2012). See Fig. 2 for locations.

92 2 A geomechanical model for reservoir-induced landslide

93 2.1 Typical reservoir-induced landslides in the Three Gorges Reservoir

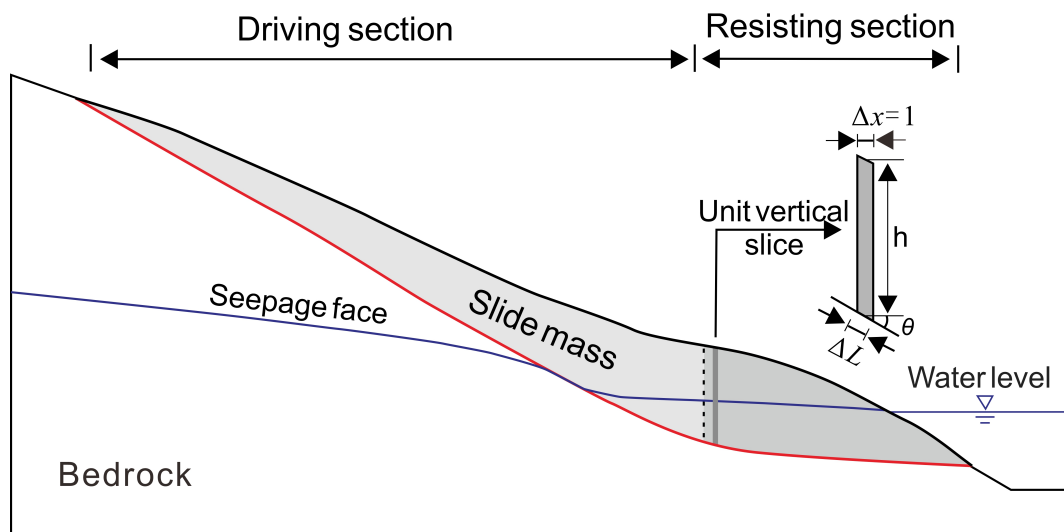
94 Figure 1 and Fig. 2 summarize the reservoir landslides of most concern in the TGR plus the
95 world famous Vajont landslide. These landslides have many common features. First, all these
96 landslides have large volumes, ranging from millions of cubic meters to tens of millions of cubic
97 meters, and all are difficult to reinforce by conventional structures such anti-slide pile, retaining wall
98 etc. Second, the front part of the slide mass is always thicker than the rear part, with a maximum
99 thickness from 40 m to over 100 m. Another important feature of these profiles (Fig. 1) is that the
100 slope of the slide surface decreases gradually from the rear to the front and may become horizontal
101 or even anti-dip in the front. Last, these landslides were reactivated after the reservoir impoundment,
102 with large observed deformations indicating their metastable situation. All these features are relevant
103 to the deformation behavior of reservoir landslides, as discussed below.



105 **Fig. 2** Location map for important landslides in TGR. Jiuxianping landslide (A); Xicheng landslide
106 (B); Outang landslide (C); Huangtupo landslide (D); Muyubao landslide (E); Baishuihe landslide (F);
107 Qiangjiangping landslide (G); Ganjuyuan landslide (H); Shuping landslide (J), Case study.

108 **2.2 Driving-resisting model**

109 Due to the relatively high slope of the slide surface in the middle and rear part, the slide force
110 exceeds the resistance force on the proximal slide surface, producing extra thrust on the lower-front
111 slide mass. Consequently, the rear-upper is termed the “driving section” (Fig. 3). In contrast, the
112 potential slide surface underlying the lower-front part of the slide mass provides more resistance due
113 to the relatively gentle slide surface slope and greater thickness of the slide mass. The lower-front
114 part of the slide mass is termed the “resisting section” (Fig. 3), as it provides main resistance force
115 for the whole slide mass, thereby playing a critical role in landslide stability (Tang et al., 2015).



116

117

Fig. 3 Driving-resisting model for reservoir landslide

118 The resisting section is defined as the lower-front part of the slide mass, where each unit vertical
119 slice (Fig. 3) can be self-stabilized under its self-weight. According to the limit equilibrium method
120 and the definition of the resisting section, the sliding force of each vertical slice is the component of
121 its gravitational force along the slide surface, which cannot exceed the shear resistance provided by
122 the base. The special position where the sliding force of the vertical slice equals the resistance force

123 provided by the slide surface is regarded as the boundary between the driving and resisting sections.

124 In the unit vertical slice of resisting section, the difference between the forces on the two vertical

125 sides is very tiny because the width of the unit vertical slice is very small, and the slide surface

126 underlying the lower-front part of the slide mass is relatively gentle; so the interslice forces were

127 ignored for the convenience of analysis. Force balance along the sliding direction for this special

128 vertical slice can be written as

129
$$w \sin \theta_1 = w \cos \theta_1 \tan \varphi + c \Delta L \quad (1)$$

130 where w is the weight of the unit vertical slice; θ_1 is the slope angle of the slide surface at the

131 boundary between the driving and resisting sections; ΔL is the length of the slice base (see Fig. 3);

132 and c and φ are the cohesion and internal friction angle of the slide surface, respectively.

133 The weight of the slice $w = \gamma h \Delta x$, where γ is the unit weight of the slide mass, h is the vertical

134 distance from the center of the base of the slice to the ground surface, Δx is the unit width of the slice,

135 and $\Delta L = \Delta x / \cos \theta_1$ (Fig. 3). Thus Eq. (1) can be rewritten as

136
$$\tan \theta_1 = f + k / \cos^2 \theta_1 \quad (2)$$

137 where $f = \tan \varphi$, $k = c / \gamma h$.

138 The solution to Eq. (2) provides the slope angle θ_1 of the slide surface:

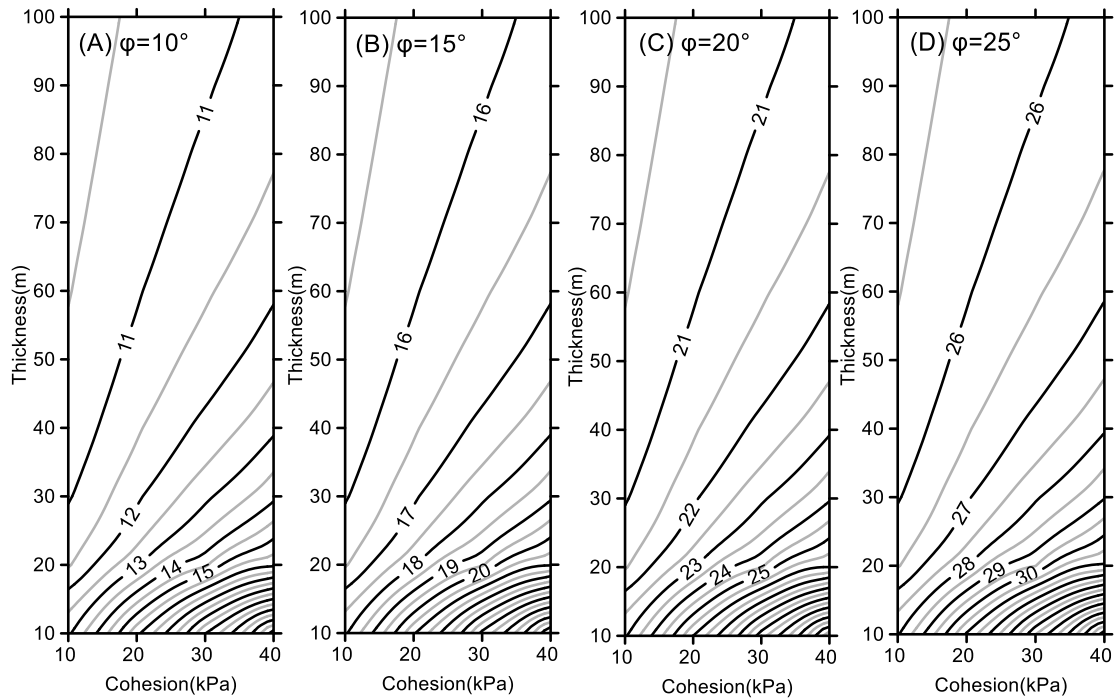
139
$$\theta_1 = 0.5 \arcsin T \quad (3)$$

140 where
$$T = \frac{(2k + f) + \sqrt{(2k + f)^2 - 4k(k + f)(1 + f^2)}}{1 + f^2}$$

141 Empirical values for the cohesion of the slide surface is less than 40 kPa, while the internal

142 friction angle of the slide surface varies between 10° and 25° (Chang et al., 2007), and the unit

143 weight of the soil is typically about 20 kN/m^3 . In order to further elucidate the effect of various
 144 parameters on the length of the **resisting** section, contour maps of θ_1 under different shear strength
 145 parameters c and ϕ and the thickness of the slide mass h are plotted (Fig. 4), as derived from Eq. (3).



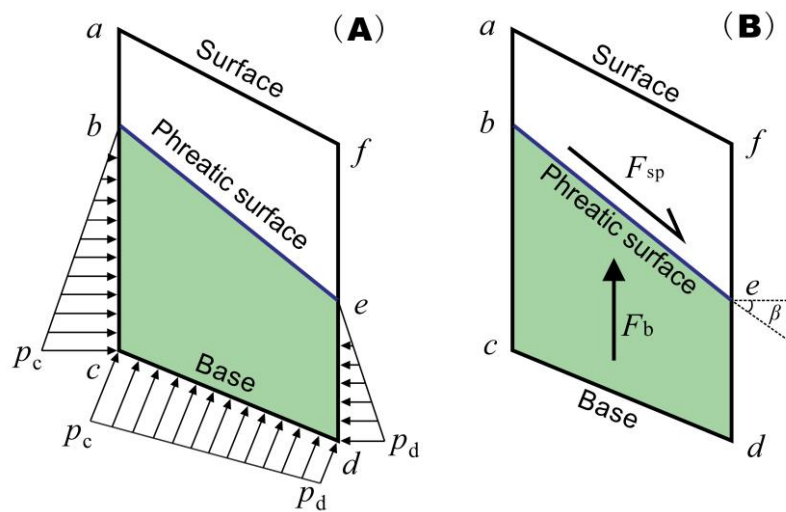
146
 147 **Fig. 4** Coutour maps for the slope angle θ_1 of slide surface that denotes the boundary between the
 148 driving and **resisting** sections under various shear strength parameters and slide mass thickness.

149 Figure 4 shows that θ_1 increases as the internal friction angle ϕ increases; however, by
 150 comparison of the pattern and the values of the contour in the four sub-figures, the difference
 151 between θ_1 and ϕ has little relationship to ϕ . Due to the effect of cohesion, θ_1 is always larger than ϕ
 152 as shown in Fig. 4. As the cohesion c decreases, the difference between θ_1 and ϕ decreases, and for
 153 cohesionless material with $c=0$, θ_1 is equal to ϕ . Fig. 4 also shows that when the thickness of the slide
 154 mass reaches about 40 m, the difference between θ_1 and ϕ is very small (less than 3°), which
 155 becomes even less as the thickness increases. These results indicate that for the thick slide mass (up

156 to 40 m), the boundary between the **resisting** and driving sections can be approximated as the
 157 position where the slope angle θ_1 equals the internal friction angle φ .

158 2.3 Effect of water force on the **resisting** and driving sections

159 The impacts of the water level change on the reservoir slope stability can be quantified by
 160 analyzing the changes in water force on the slope. Lambe and Whitman (2008) have demonstrated
 161 that the water forces acting on an element of the slope can be equivalently expressed by either the
 162 ambient pore-water pressure (Fig. 5A) or by seepage and buoyancy forces (Fig. 5B). The latter form,
 163 i.e., seepage and buoyancy forces, are employed here to clarify the mechanical mechanism of water
 164 force on the reservoir bank.



165
 166 **Fig. 5** Two equivalent ways to display the water force acting on a slice of the slide mass. (A)
 167 expressed by pore-water pressure; (B) expressed by the seepage force F_{sp} and the buoyancy force F_b .

168 The seepage force (F_{sp}) represents the frictional drag of water flowing through voids that is
 169 proportional to the hydraulic gradient and acts in the direction of flow. It can be expressed as (Lambe
 170 and Whitman, 2008)

171
$$F_{sp} = \gamma_w i V \quad (4)$$

172 Where γ_w is the unit weight of water; i is the hydraulic gradient and equals $\sin\beta$ where β is the slope
 173 angle of the phreatic surface; V is the submerged volume of the analyzed element as the trapezoid
 174 area enclosed by points bcd e in Fig. 5.

175 When the groundwater flows outwards as occurs during reservoir level drops, the corresponding
 176 outward seepage force decreases the slope stability. In contrast, the seepage force will be directed
 177 inward during reservoir level rise, increasing slope stability.

178 The buoyancy force (F_b) of the water exerted on the element can be expressed as

179
$$F_b = \gamma_w V \quad (5)$$

180 The factor of safety (Fos) used to quantify the slope stability can be defined as the ratio of the
 181 shear strength (resistance, F_r) along the potential failure surface to the sliding force (F_s) by the
 182 Mohr-Coulomb failure criterion (Wang et al., 2014):

183
$$Fos = \frac{F_r}{F_s} = \frac{\sum_{j=1}^n [c\Delta L_j + N_j \tan \varphi]}{\sum_{j=1}^n w_j \sin \theta_j} \quad (6)$$

184 where n is the total number of slices; N is the normal force on the base of each slice, and the other
 185 symbols are as above. Suppose that the variation of the effective slide mass weight in a slice is Δw ,
 186 due to the change of buoyancy force, which thereby modifies the resistance and sliding forces by ΔF_r
 187 and ΔF_s respectively. The corresponding change of the factor of safety ΔFos is:

188
$$\Delta Fos = \frac{F_r + \Delta F_r}{F_s + \Delta F_s} - \frac{F_r}{F_s} = \frac{\Delta F_r * F_s}{(F_s + \Delta F_s) F_s} \left(1 - \frac{Fos}{\Delta F_r / \Delta F_s} \right) \quad (7)$$

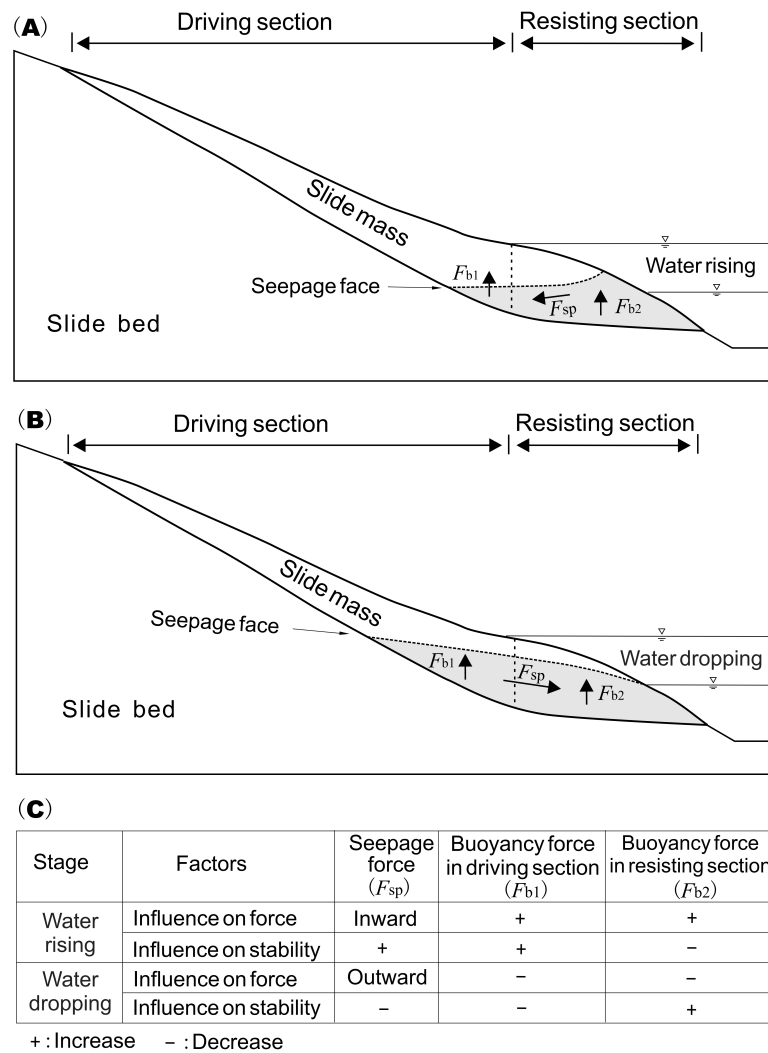
189 The ratio of ΔF_r to ΔF_s for a vertical slice due to the change of its effective weight Δw is

190 approximately:

$$191 \quad \frac{\Delta F_r}{\Delta F_s} = \frac{\Delta w \cos \theta \tan \varphi}{\Delta w \sin \theta} = \frac{\tan \varphi}{\tan \theta} \quad (8)$$

192 Suppose that $\theta_2 = \arctan\left(\frac{\tan \varphi}{F_{os}}\right)$, where the change of the vertical slice weight has no influence
193 on the current stability ($\Delta F_{os}=0$). If $\theta < \theta_2$ and $\Delta w > 0$, then $\Delta F_{os} > 0$, indicating that increase of the
194 weight of lower-front part of the slide mass where its slope angle of the slide surface θ is less than θ_2
195 will improve the stability of the whole slide mass; conversely, decrease of the weight of the
196 lower-front part would decrease stability. In contrast, the upper-rear part has a contrary tendency. As
197 mentioned above, continuously deformed reservoir landslides are metastable and their corresponding
198 F_{os} is around 1; hence $\theta_2 \approx \varphi$. Consequently, in the cases that reservoir landslide is under metastable
199 state and has a thickness up to 40 m, $\theta_1 \approx \theta_2 \approx \varphi$, the **resisting** section and driving section have the same
200 mechanical behavior as described above. Either an increase in the weight of the **resisting** section or a
201 decrease in the weight of the driving section will improve the stability of the slope and vice versa.

202 In summary, the effect of ground water on the slope or landslide stability can be resolved into a
203 seepage force and a buoyancy force. The effect of the seepage force on slope stability depends on the
204 direction and magnitude of flow. Buoyant forces change the effective weight of the slide mass and
205 have contrary effect on the **resisting** and driving sections. On the basis of these rules, the mechanical
206 mechanism for reservoir-induced landslide can be illustrated as Fig. 6.



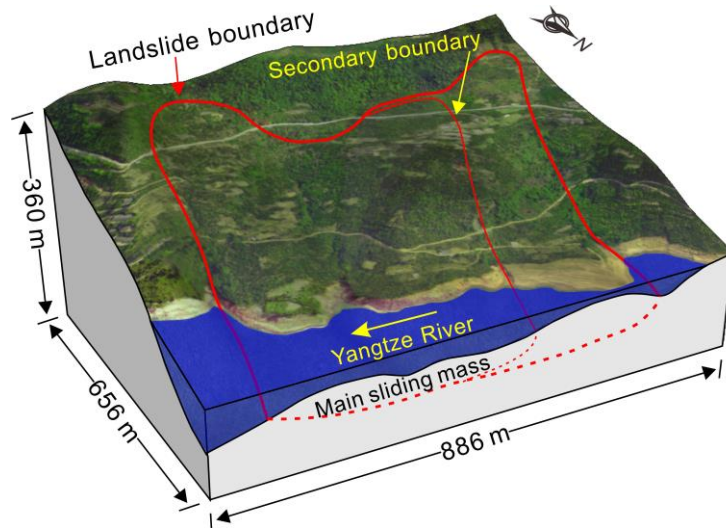
207

208 **Fig. 6** Mechanical mechanism for reservoir-induced landslide. (A) water level rise; (B) water level
 209 drop; (C) effects of various mechanisms on the landslide stability during water level rise and drop.

210 **3 Shuping landslide**

211 Shuping landslide is located in Shazhenxi Town, Zigui County, Hubei Province, on the south
 212 bank of the Yangtze River, 47 km upstream from the Three Gorges dam (Fig. 2). After the first
 213 impoundment of the reservoir in 2003, serious deformation was observed that endangered 580
 214 inhabitants and navigation on the Yangtze River (Wang et al., 2007). Previous studies of the Shuping
 215 landslide utilized GPS extensometers (Wang et al., 2007), or field surveys (Lu et al., 2014) to clarify

216 the deformation. This study provides a detailed geomechanical model that includes seepage and
217 buoyancy effects to clarify the deformation mechanism of this landslide which is calibrated by
218 long-term monitoring data.



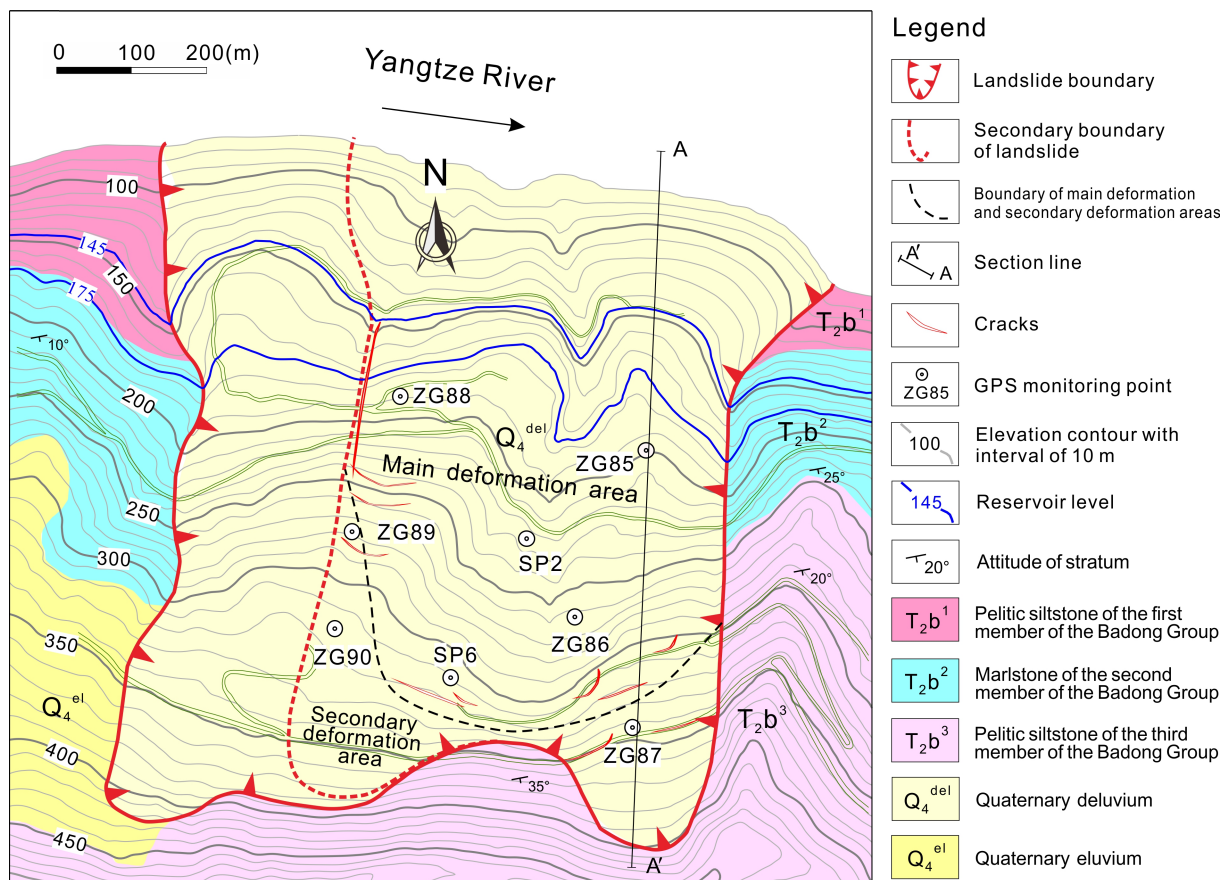
219

220 **Fig. 7** Full view of Shuping landslide (the surface satellite map © Google Maps).

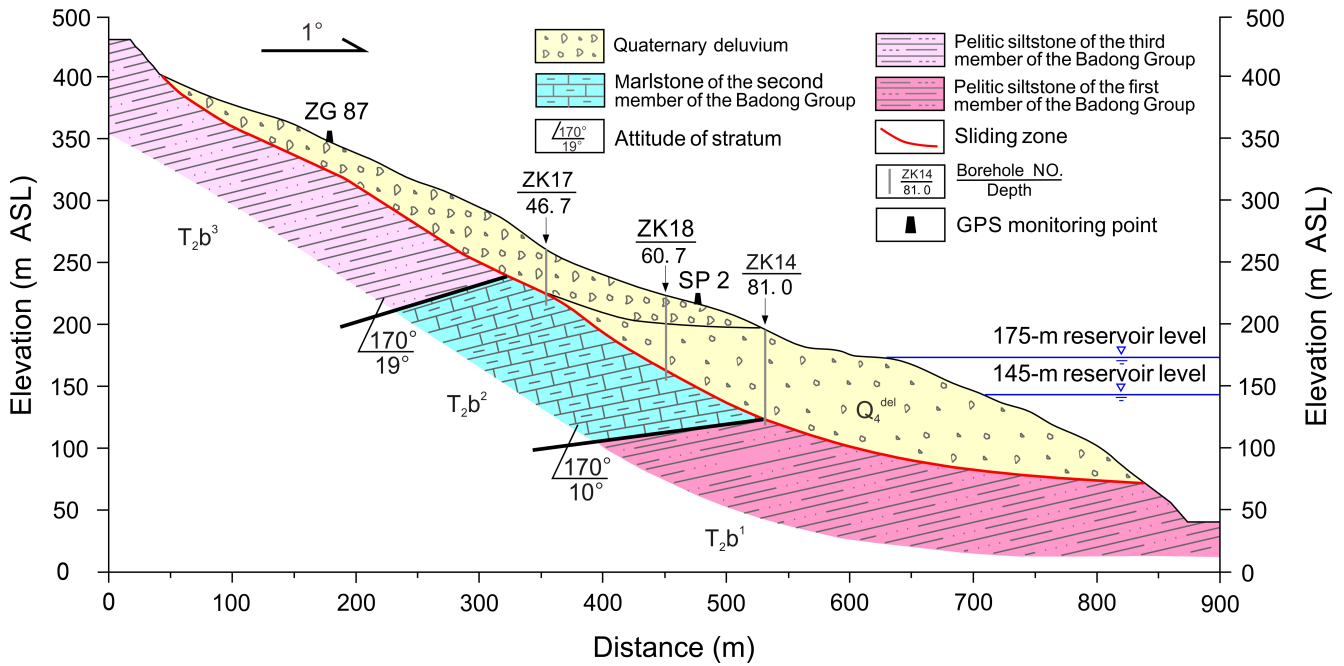
221 3.1 Geological setting

222 The Shuping landslide is a chair-shaped slope that dips 20° to 30° to the north, toward the
223 Yangtze River (Fig. 7). The landslide is bounded on the east and west by two topographic gutters.
224 The altitude of its crown is 400 m above sea level (ASL), while its toe is about 70 m ASL, which is
225 now submerged by the reservoir, level of which varies annually between 145 and 175 m ASL (Fig. 8).
226 Borehole and inclinometer data (Lu et al. 2014) indicate that there are two major slide surface within
227 the west part of the slope and the upper rupture zone divides the slide mass into two parts (see Fig. 7).
228 The whole slide mass has a thickness of 30-70 m, a N-S length of about 800 m and W-E width of
229 approximately 700 m, constituting a total volume of ~ 27.5 million m^3 , of which 15.8 million m^3
230 represents the main slide mass.

231 Shuping landslide is situated on an anti-dip bedrock of marlstone and pelitic siltstone of the
 232 Triassic Badong Group (T_2b) (Fig. 9). The upper part of the slide mass is mainly composed of yellow
 233 and brown silty clay with blocks and gravels, while the lower part of the slide mass mainly consists
 234 of dense clay and silty clay with gravels, with a thickness of about 50 m on average. The deep
 235 rupture zone is a 0.6~1.7 m layer that extends along the surface of bedrock, and consists of
 236 yellowish-brown to steel gray silty clay. The upper rupture zone in the west part has similar
 237 composition and has an average thickness of 1.0-1.2 m. The dip angle of the slide surface decreases
 238 gradually from the rear to the front (Fig. 9), so the driving-resisting model is appropriate for Shuping
 239 landslide. Before reservoir impoundment, boreholes ZK17 and ZK18 were dry but borehole ZK14
 240 contained groundwater near the rupture zone.



241
 242 **Fig. 8** Engineering geology map of Shuping landslide



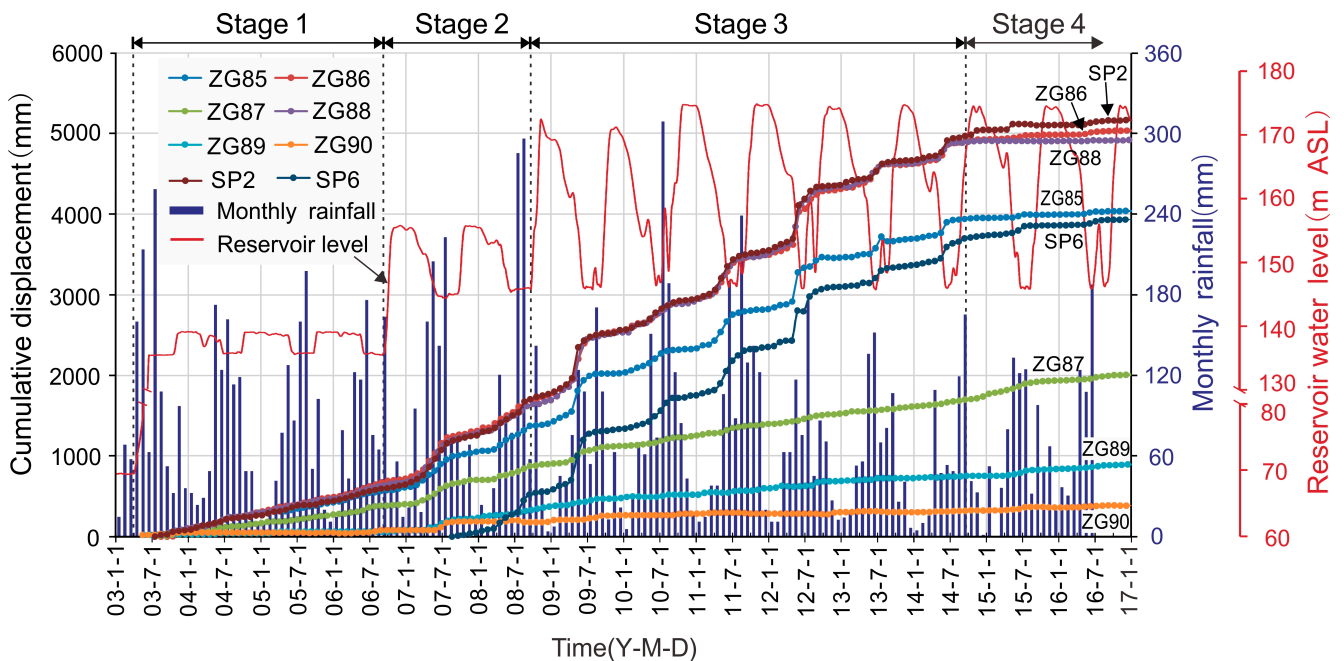
243
244 **Fig.9** Geological profiles along section A-A' as shown in Fig. 8

245 **3.2 Monitoring instrumentation**

246 The displacement monitoring system of Shuping landslide consists of 11 global positioning
 247 system (GPS) survey points, three of which are datum marks that were installed on stable ground
 248 outside the landslide area with the remainder being on the main slide mass (Fig. 8). Seven of the GPS
 249 monitoring points (SP2, ZG85, ZG86, ZG87, ZG88, ZG89 and ZG90) were set in June 2003 and
 250 GPS monitoring points SP6 was set in August 2007. All the GPS monitoring points were surveyed
 251 every half month, and the system was upgraded to automatic, real-time monitoring in June 2012. The
 252 daily rainfall records are obtained from the Meteorological Station near the Shuping landslide. Daily
 253 reservoir level is measured by China Three Gorges Corporation (source:
 254 <http://www.ctg.com.cn/inc/sqsk.php>).

255 **3.3 Engineering activity**

256 The evolution of Shuping landslide is related to four stages of human activity (Fig. 10). The first
 257 stage was the 139 m ASL trial reservoir impoundment (from April 2003 to September 2006). The
 258 reservoir water level was lifted from 69 to 135 m ASL and then changed between 135 and 139 m
 259 ASL. The second stage was 156 m ASL trial reservoir impoundment (from September 2006 to
 260 September 2008). The reservoir water level was raised from 139 to 156 m ASL, and then varied
 261 annually between 145 and 156 m ASL. The third stage was 175 m ASL trial reservoir impoundment.
 262 This stage began when the reservoir water level was raised to 175 m ASL, and thereafter managed to
 263 annually varied between 145 and 175 m ASL (Tang et al., 2019). During the fourth stage, an
 264 engineering project for controlling the deformation of Shuping landslide was conducted in
 265 September 2014 and completed in June 2015 (see Section 6 for detailed description).

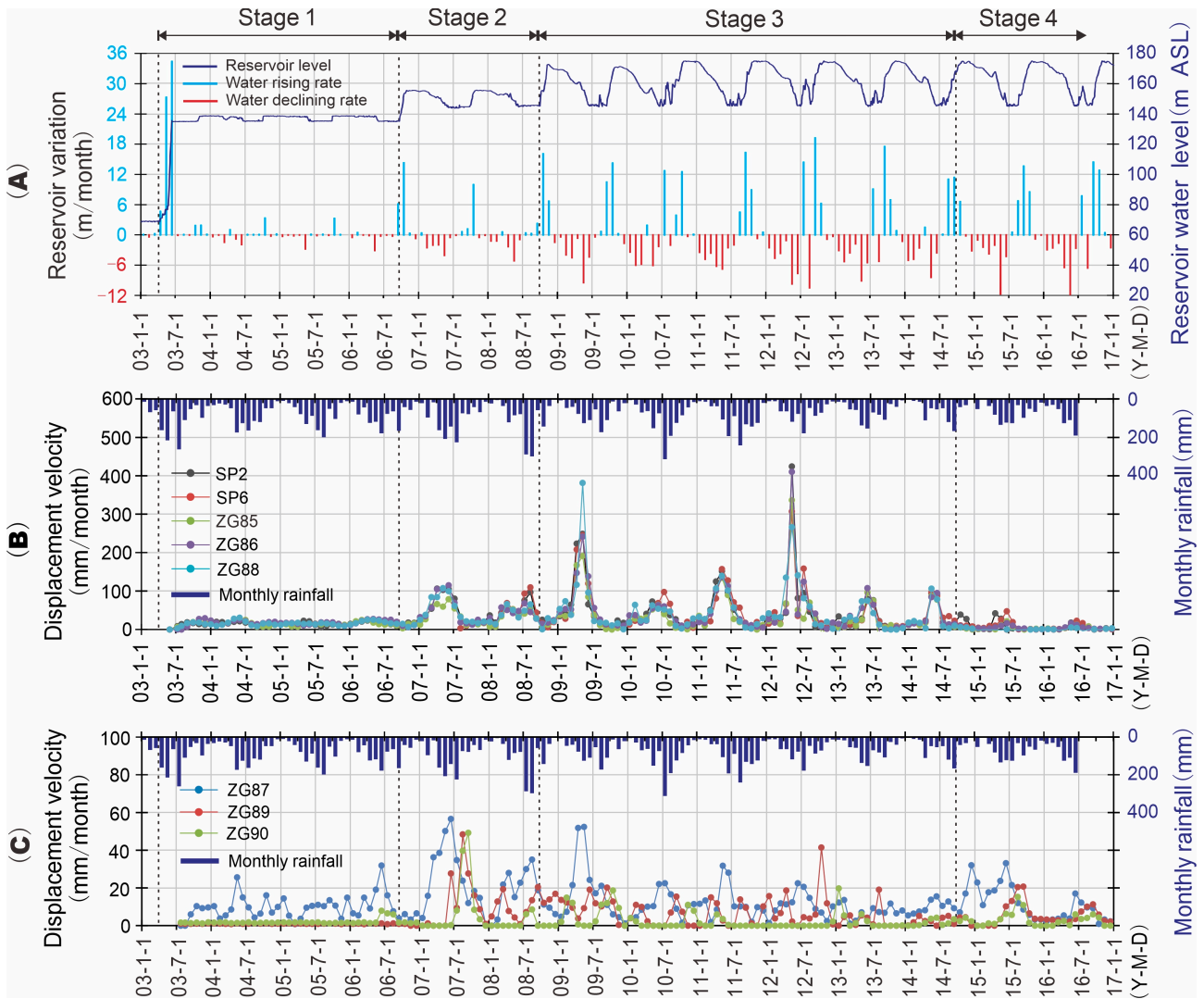


266 **Fig. 10** Monitoring data for Shuping landslide from 2003 to 2016.

268 **4 Field observational results**

269 **4.1 Overall deformation feature**

270 According to the deformation features revealed by the GPS monitoring system (Fig. 10, Fig. 11)
271 and field investigations, the main slide mass can be divided into a main deformation area and a
272 secondary deformation area (Fig. 8). The main deformation area underlies most of the area and has a
273 cumulative displacement up to 4-5 m, as measured at sites ZG85, ZG86, ZG88, SP2 and SP6. During
274 the 13-year monitoring period point SP2 underwent the largest cumulative displacement (5.168 m),
275 followed by ZG86 and ZG88 which recorded 5.039 m and 4.919 m, respectively. Deformations were
276 essentially synchronous at the monitoring sites as indicated by the similar shape of their cumulative
277 displacement curves, which typically show steady rises in the first impoundment stage, step-like
278 trends in the second and third impoundment stages, and flat trends after the engineering treatment.
279 Deformations were smaller and steadier in the secondary deformation area, as indicated by gentle
280 cumulative displacement curves at ZG89, ZG90, and ZG87, which recorded cumulative
281 displacements of 0.5-2 m during 2003 to 2016.



282

283 **Fig. 11** Time series of reservoir level, rainfall and landslide displacement from 2003 to 2016. (A)
 284 Reservoir water levels and variation rates (positive for level rise, negative for level drop); (B)
 285 **Displacement** velocity of the GPS points in the main deformation area and monthly rainfall; (C)
 286 **Displacement** velocity of the GPS points in secondary deformation area and monthly rainfall.

287 **4.2 Deformation feature in different stages**

288 After the reservoir level first rose to 135 m ASL in June 2003, the main deformation area
 289 deformed at an average velocity of 15.6 mm/month until September 2006, with each site recording
 290 rather steady displacement curves whose tiny or nonexistent steps correspond to the small annual

291 variations in reservoir level. In contrast, no obvious deformation occurred during Stage 1 at ZG89
292 and ZG90 in the secondary deformation area.

293 During the earliest two months of Stage 2 (September, October 2006), when the reservoir level
294 first rose to 156 m ASL, **displacement** velocities of the main deformation area decreased to 13.4 and
295 9.7 mm/month respectively, indicating that slide mass stability had improved. For the next two
296 months (November, December) the velocity increased to 11.5 and 14.3 mm/month, as the reservoir
297 level was steady at 156 m ASL. During the subsequent drawdown period when the reservoir level
298 dropped to 145 m ASL in 2007, the **displacement** velocity increased to a maximum of about 100
299 mm/month (Fig. 11), resulting in an average “jump” of 458 mm in the cumulative displacement
300 curve, which then became flat while the reservoir remained at 145 m (Fig. 10).

301 During the beginning of Stage 3 when the reservoir first rose to nearly 175m in October 2008,
302 the **displacement** velocity of the main deformation area decreased to 12.7 mm/month, compared to
303 65, 74, 32 mm/month in the previous three months. Shortly after the reservoir rose to its highest level,
304 the level underwent a gradual decline and the **displacement** velocity increased steadily. The
305 maximum **displacement** velocity reached 378.6 mm/month at ZG88 in May 2009 when the water
306 level declined rapidly, a rate almost four times higher than when the reservoir dropped from 156 to
307 145 m ASL in 2007. Then the **displacement** velocity decreased to a relatively low value when the
308 water level was steady at 145 m ASL (Fig. 11B).

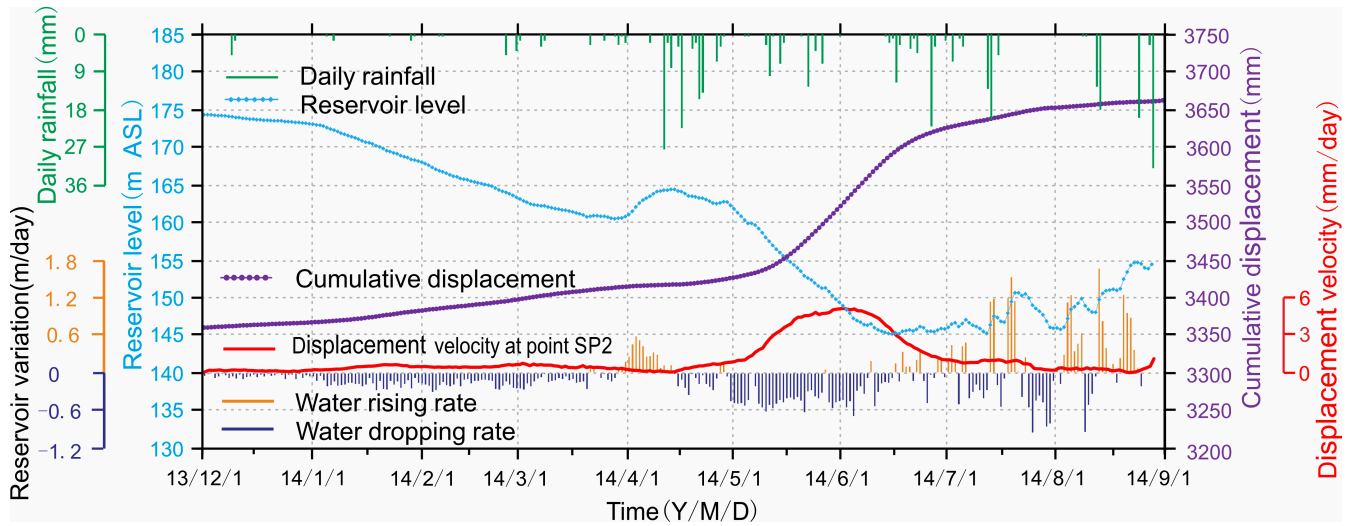
309 In the subsequent 6 years of Stage 3 the reservoir level underwent a series of similar annual
310 variations, and the slide mass responded with a series of deformation “jumps”. During these cycles,

311 the **displacement** velocity decreased as the reservoir rose, maintained low values when the reservoir
312 remained high, began to increase as drawdown began, and attained the values up to 165 mm/month
313 when drawdown was rapid. The corresponding cumulative **displacement** curves featured obvious
314 “jumps” during drawdown periods, then became relatively flat as the reservoir was maintained at the
315 low level of 145 m ASL. Clearly, these results show that **displacement** velocity is high during
316 reservoir drawdown and low during reservoir rise.

317 After the engineering treatment was completed in June 2015, the “jumps” in the cumulative
318 displacement curves disappeared and the curves became very flat (Fig. 10). The deformation was
319 reduced to a low level of 4.1 mm/month in the main deformation area, demonstrating effective
320 treatment.

321 **4.3 Effect of water-level fluctuation and rainfall on the deformation of Shuping landslide**

322 The largest “jump” in the cumulative displacement curves averaged 479 mm and occurred in
323 May to June, 2012, while the second was the jump of 458 mm in May to June, 2009. These periods
324 corresponded with the two highest drawdown rates of 9.67 and 9.38 m/month, respectively (Fig.
325 11A). During these two years, rainfall amounts were relatively low with monthly maxima of 180
326 mm/month in 2009 and 190 mm/month in 2012 (Fig. 11). These data clearly demonstrate that the
327 deformation of Shuping landslide is primarily driven by reservoir level variations and not by rainfall.
328 This relationship is also confirmed by the low **displacement** velocities and flat cumulative
329 displacement curves during the July and August peak of the rainy season, when the reservoir is held
330 at its lowest level.



331
 332 **Fig. 12** Monitoring data of GPS point SP2 on the middle part of slide mass, from December 2013 to
 333 September 2014.

334 Figure 12 clarifies the influence of reservoir level and rainfall on landslide deformation. In
 335 December 2013, the reservoir level dropped at an average rate of 0.041 m/day, and the corresponding
 336 **displacement** velocity was 0.22 mm/day. In the subsequent three months, the drawdown rate of the
 337 reservoir level increased to 0.147 m/day, and the **displacement** velocity rose to 0.54 mm/day. During
 338 March 2014, the **displacement** velocity decreased as the water level increased, even though intense
 339 rainfalls were recorded during this period (up to 27.5 mm/day). In the following rapid drawdown
 340 period (0.419 m/day) from May to June, the **displacement** velocity increased to about 5 mm/day.
 341 Subsequently, the **displacement** velocity decreased to less than 1.2 mm/day as the water level
 342 remained low, although rainfall was abundant. These details confirm that the **displacement** velocity
 343 of the Shuping landslide is positively related to the drop rate of the reservoir, with rainfall having
 344 little effect.

345 Unlike the flat displacement curves and low **displacement** velocity in other years when the
 346 reservoir level was steady at the lowest annual level in July and August, **displacement** velocities were

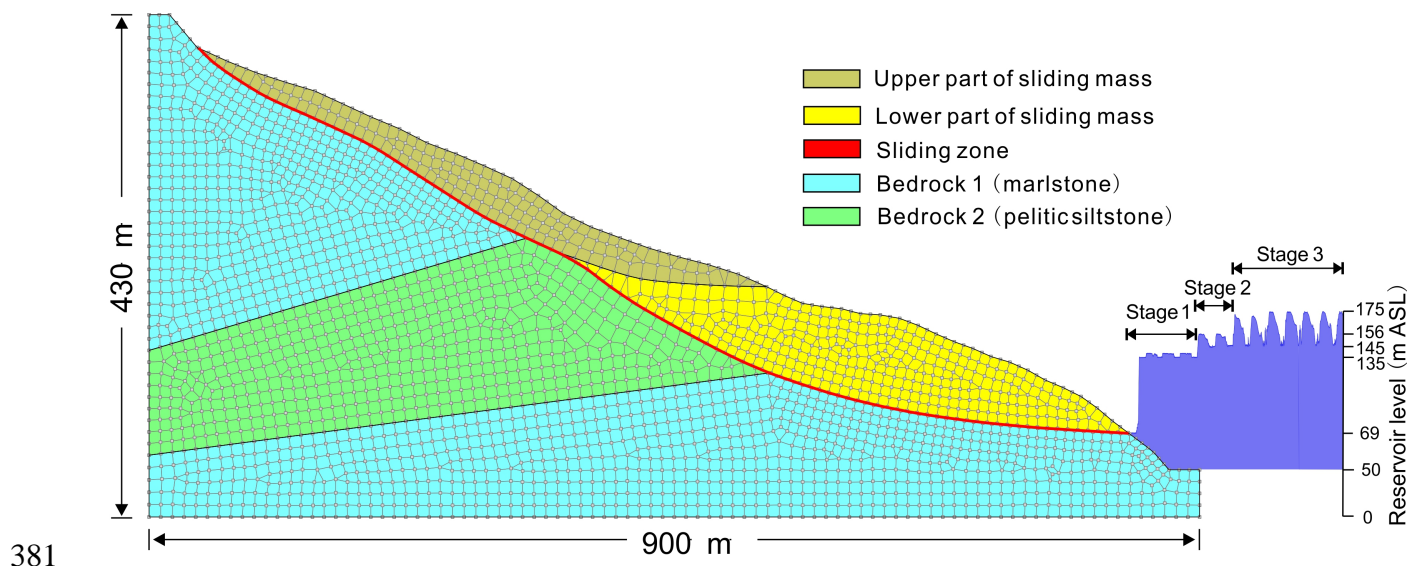
347 large in 2008 and 2010 (65.0 and 73.8 mm/month in July and August 2008; 58.4 mm/month in July
348 2010, about half of the average highest monthly displacement velocity, 165 mm/month, during rapid
349 draw down period). Very heavy rainfall was recorded during those periods, up to 300 mm/month.
350 However, August 2011 had the next heaviest rainfall of 250 mm/month, yet the cumulative
351 displacement curve remained flat and the displacement velocity was low (22.2 mm/month). These
352 data illustrate that heavy rainfall can decrease landslide stability and accelerate deformation, but
353 nevertheless is a secondary factor. The difference in the displacement velocity between the months
354 with the highest (2008, 2010) and the second highest (2011) levels of rainfall suggests that a
355 threshold exists, with rainfall exceeding this value having a significant effect but with less having
356 little significance. This threshold appears to be about 250-300 mm/month.

357 **5 Numerical simulation**

358 In this section, groundwater flow in the Shuping slope under the variation of the reservoir level
359 is simulated to assist the driving-resisting model to explain the deformation process of Shuping
360 landslide. Seepage simulation is performed by the SEEP/W module of GEOSTUDIO software (see
361 <http://www.geoslope.com>). The deformation state of the landslide is usually regarded as the
362 performance of the landslide stability state (Wang et al., 2014; Huang et al., 2017). Thus, the *Fos*
363 (Safety of factor) of the Shuping landslide is calculated with the simulated groundwater level, to
364 evaluate the stability of the Shuping landslide under various impoundment scenarios. In this study,
365 the *Fos* of the Shuping landslide is calculated by Morgenstern-Price method (Zhu et al., 2005) using
366 the SLOPE/W module of GEOSTUDIO software. The external impoundment load affect is

367 considered by this software. Different evaluation method for landslide stability will lead to different
368 value of Fos ; thus we only employ the calculated values of Fos to investigate the variation trend of
369 the landslide stability.

370 Figure 13 shows the numerical simulation model of the Shuping landslide, whose framework is
371 based on the geological profile map in Fig. 9. The slope was divided into six regions composed of
372 five materials with different properties (Table 1). Zero flux boundary conditions were assigned along
373 the bottom horizontal and the right vertical boundaries. A constant water head was applied at the left
374 vertical boundary assuming that it is sufficiently far from the reservoir to not be affected by
375 reservoir-level variations. A series of inverse modelling tests and water tables at the boreholes were
376 adopted to determine the constant water head at the left vertical boundary. The optimum water head
377 at the left boundary is 230 m ASL. The hydrograph of TGR from January 1, 2003 to September 10,
378 2014 (Fig. 14(A)) and generalized hydrograph of the trial impoundment at 175 m ASL (Fig. 14(B))
379 were used to define the right boundary adjacent to the reservoir. Initial conditions were defined using
380 the water tables revealed by boreholes.



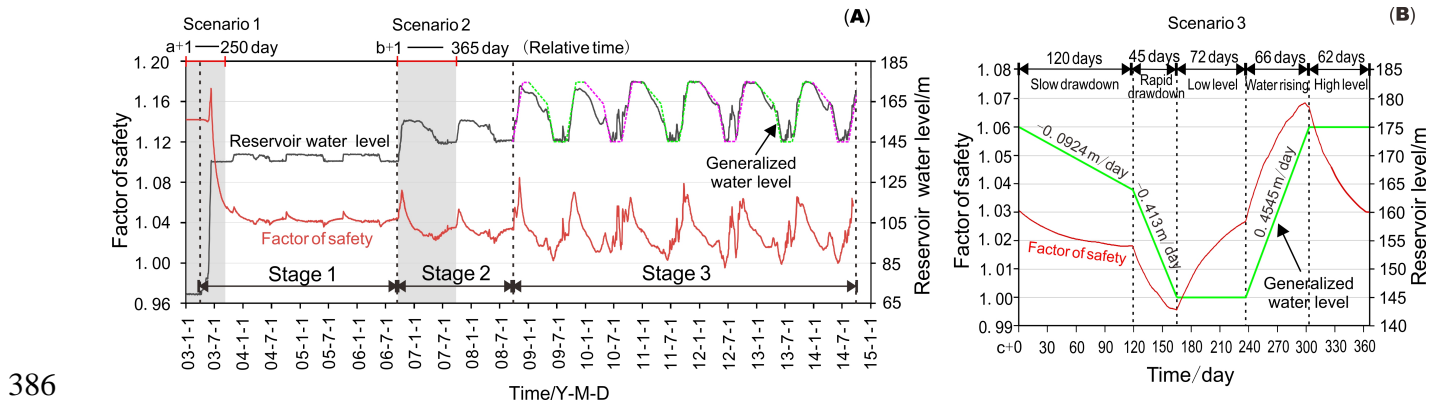
382 **Fig. 13.** Numerical simulation model of seepage for Shuping landslide.

383 **Table 1** Hydrologic and mechanical properties of Shuping landslide

Location	Material	Saturated conductivity k_s (m/day)	Residual volumetric water content θ_r	Saturated volumetric water content θ_s	Fitting parameter in the van Genuchten's model α	Fitting parameter in the van Genuchten's model n	Unit weight γ (kN/m ³)	cohesion c' (kPa)	friction angle ϕ' (°)
Upper part of slide mass	Silty clay with blocks and gravels	4.95 ^a	0.129	0.39	0.141	1.869	20.3 ^a	/	/
Lower part of slide mass	Silty clay with gravels	3.90 ^a	0.129	0.39	0.141	1.869	20.3 ^a	/	/
Rupture zone	Silty clay	2.98×10^{-2} ^b	0.08	0.30	0.035	1.758	/	25.7 ^a	20.4 ^a
Bedrock 1	Marlstone	1.47×10^{-4} ^b	0.05	0.20	0.0173	1.606	/	/	/
Bedrock 2	Pelitic siltstone	8.99×10^{-5} ^b	0.05	0.20	0.0173	1.606	/	/	/

384 ^a Provided by Hubei Province Geological Environment Terminus (2003)

385 ^b Values of similar material from literature (Hu et al., 2015)

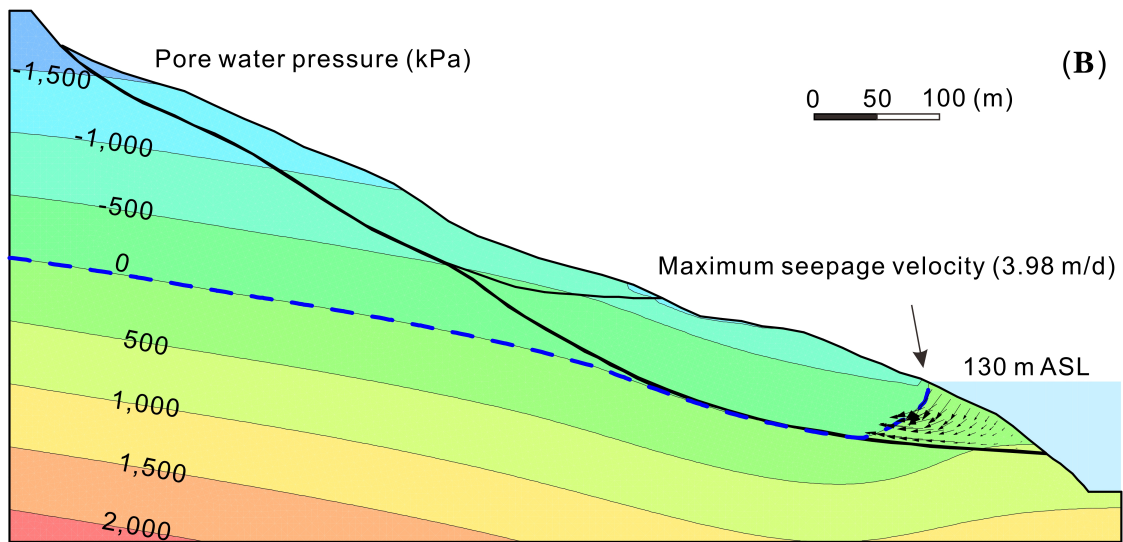
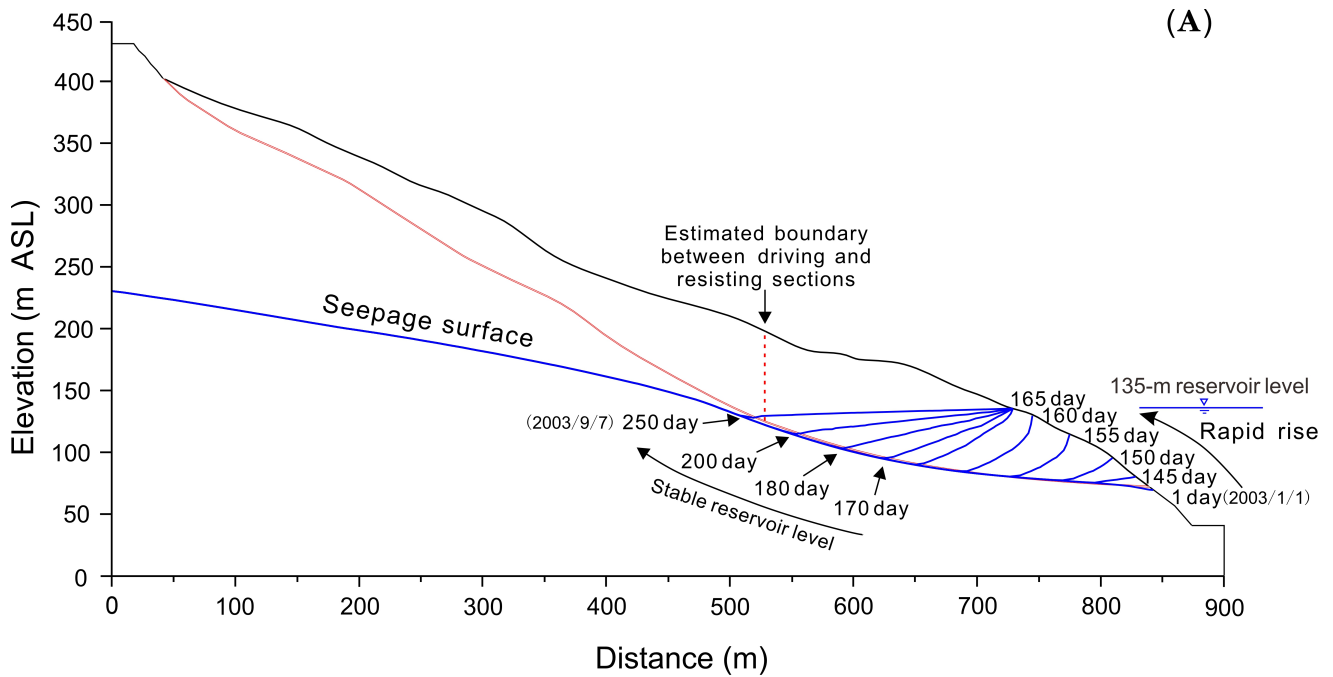


387 **Fig. 14** (A) Time series of reservoir level and corresponding calculated Fos of Shuping landslide

388 from January 1, 2003 to September 10, 2014. (B) Generalized annual variation curve of the reservoir
389 level obtained by fitting the real water level from 2008 to 2014 (Stage 3) and the corresponding time
390 series of the calculated Fos of Shuping landslide.

391 **5.1 Scenario 1: first trial impoundment at 139 m ASL**

392 From April 10 to June 11, 2003 (a+100~162 day), the reservoir level rose rapidly from 69 to 135
393 m ASL. Fig. 15 shows that, during this period, groundwater storage increased in the toe of the slide
394 mass and within the lower part of the **resisting** section, increasing buoyancy forces that destabilized
395 the slope. In contrast, the inwardly-directed flow created a seepage force directed towards the slope
396 **(Fig.15(B))**, increasing stability. Owing to the high hydraulic gradient, the stabilizing effect of the
397 seepage force on the slope prevails over the destabilization due to increased buoyancy, so slope
398 stability was improved during this phase, as indicated by the increase in Fos up to 1.17 (Fig. 14).



399
 400 **Fig. 15** (A) Simulated groundwater tables during the period of rapid reservoir rise from January 1,
 401 2003 to September 7, 2003; (B) simulated pressure contours and flow vector on June 19, 2003
 402 (a+170 day) during first impoundment period.

403 In the following period (a+163 day~), the reservoir level was maintained around 135 m ASL.
 404 The water table progressively rose until it approximated the reservoir level. During this period, the
 405 slope of the water table front decreased gradually (Fig. 15(A)), leading to the decrease of the seepage
 406 force in the slope. At the same time, the buoyancy uplift effect increased steadily in the resisting

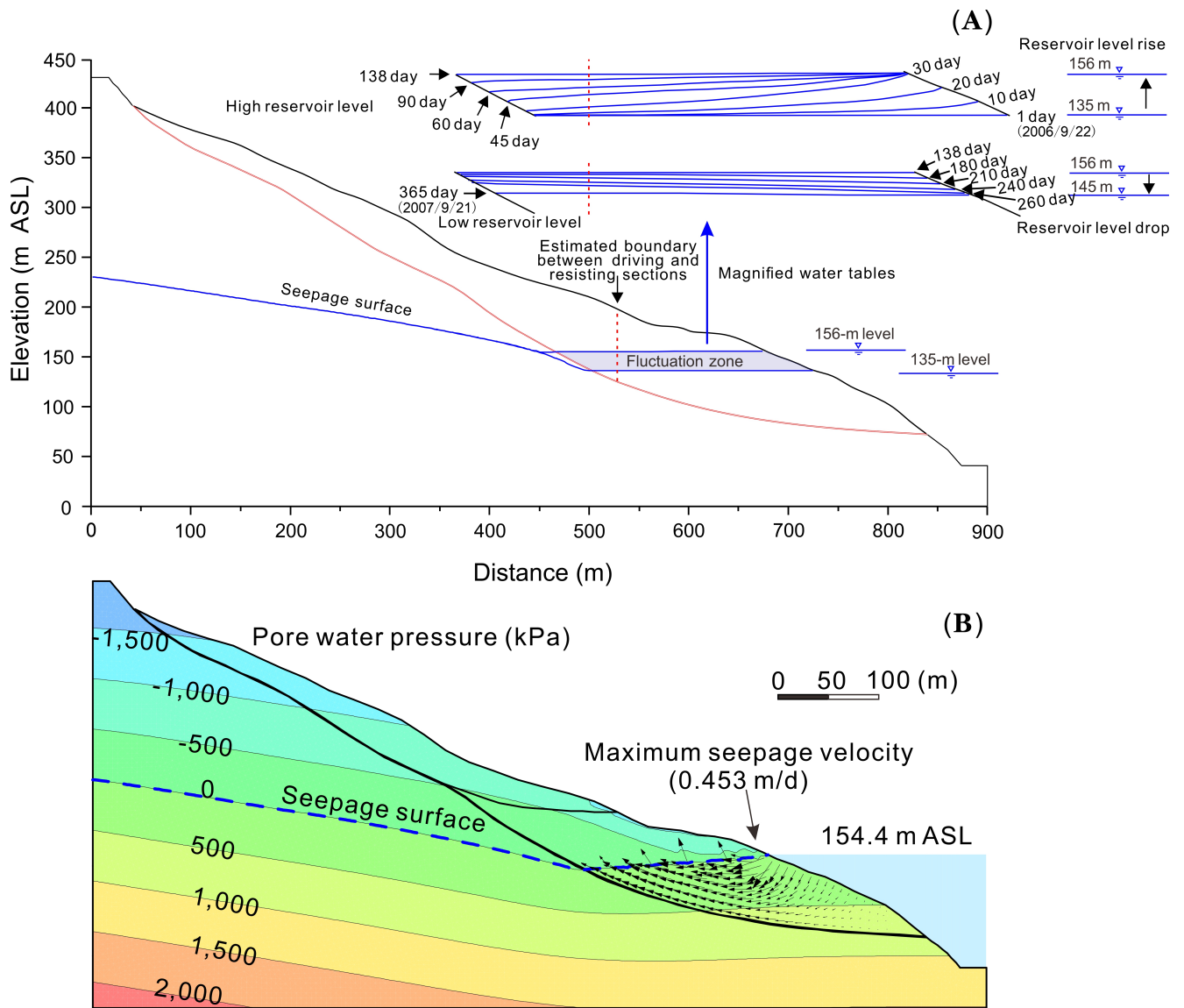
407 section as the groundwater table rose. The combination of a decreased seepage force and the
408 increased buoyancy led to a decrease in slope stability during this phase, so the Fos dropped below
409 its initial value of 1.142. Afterwards, the slope stability continued to decrease until the new but
410 temporary state of equilibrium was reached. The safety factor was around 1.045 as the reservoir level
411 was maintained around 135 m ASL.

412 The delay between the reservoir impoundment and the decrease in stability is consistent with the
413 creation of obvious cracks after the reservoir rose to 135 m ASL (Wang et al., 2007). The famous
414 Qianjiangping landslide (Fig. 2), which is located near the Shuping landslide and has similar
415 geological setting, occurred one month (13 July 2003) after the reservoir first rose to 135 m ASL
416 (Xiao et al., 2007).

417 **5.2 Scenario 2: first trial impoundment at 156 m ASL**

418 During the periods when the water level rose from 135 m ASL to 156 m ASL (b+1~30 day) (Fig.
419 16), and stayed stable at 156 m ASL (b+30~138 day), the effects of ground water level change on the
420 stability of Shuping landslide were similar to the effects in scenario 1. When the reservoir level
421 dropped from 156 to 145 m ASL during the drawdown period of February to June (b+138~260 day),
422 groundwater flow towards the reservoir (Fig. 16(B)), thus creating an outward, destabilizing seepage
423 force on the slope. The computed factor of safety decreased gradually from 1.070 to 1.025, in
424 agreement with the observed increase in displacement velocity during this period. As the reservoir
425 level was then maintained at 145 m ASL (b+260~365 day), the transient seepage gradually
426 transitioned to steady-state seepage, accompanied by a progressively decline of the water table in the

427 inside part of the fluctuation zone, a weakening of the destabilizing effect of the seepage force, and a
 428 result of increase in slope stability ($Fos=1.035$).



429
 430 **Fig. 16 (A)** Simulated groundwater tables as the variation of reservoir water level from 22 September
 431 2006 to 21 September 2007; **(B) simulated pressure contours and flow vector on July 11, 2007 (day**
 432 **b+260) during drawdown period**

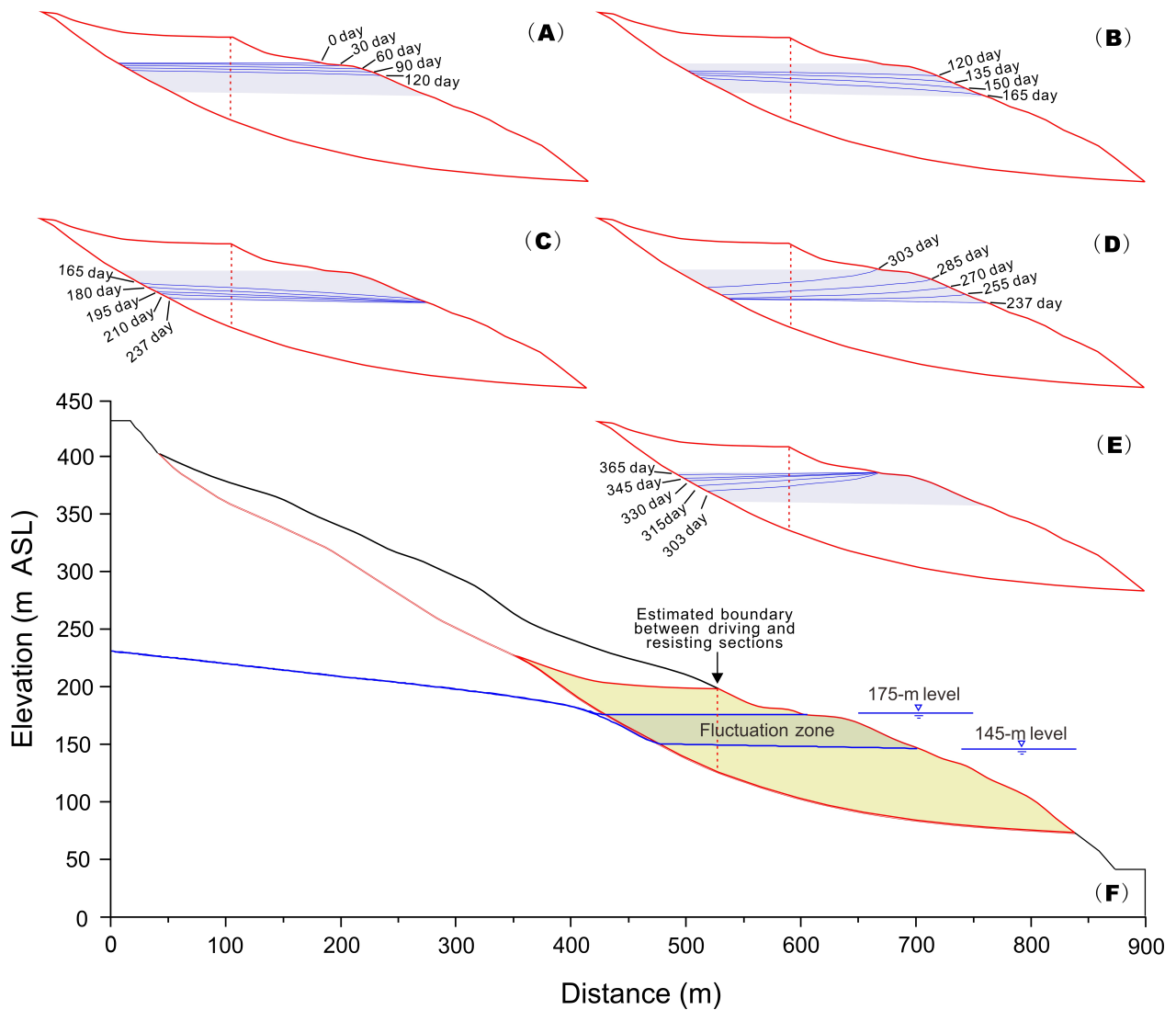
433 **5.3 Scenario 3: trial impoundment at 175 m ASL**

434 During 2008 to 2014 the reservoir level periodically fluctuated between 145 and 175 m ASL
 435 (Stage 3), in accordance with a generalized annual water level variation curve that consists of five

436 phases (Fig. 13(B)).

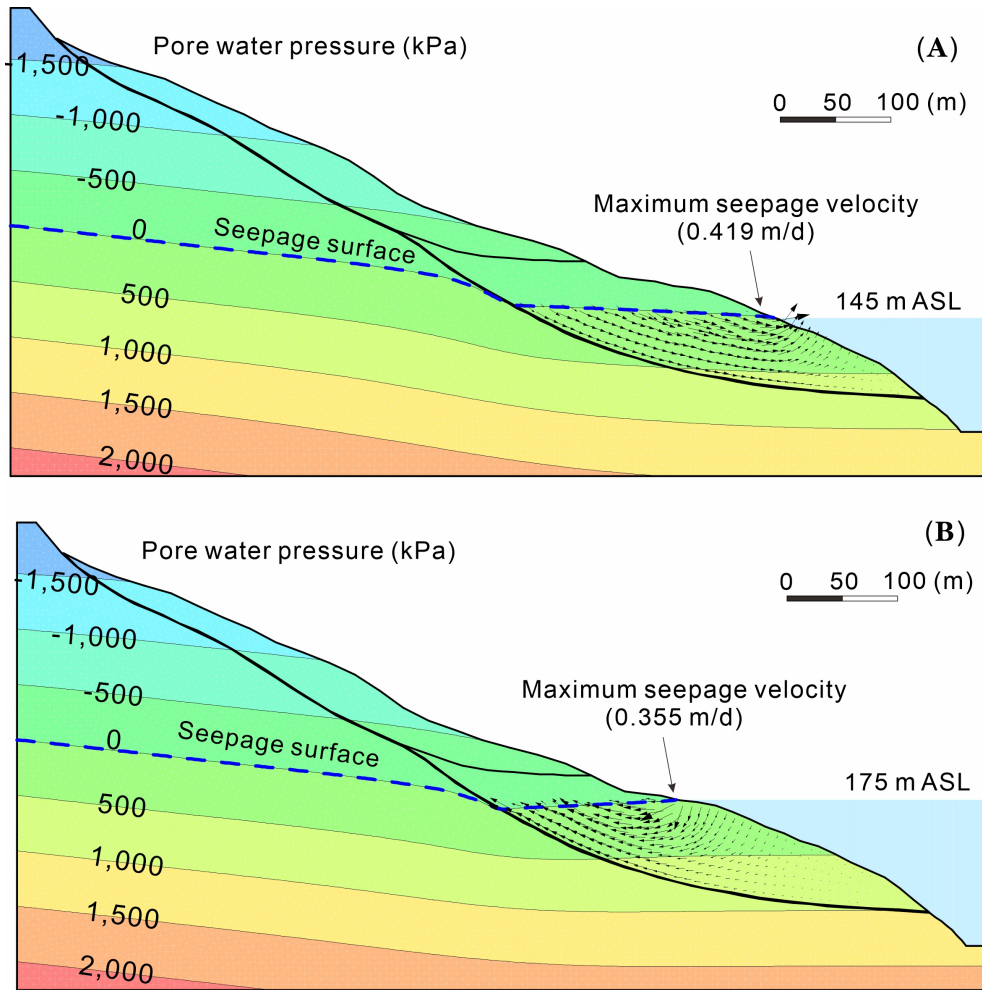
437 During the slow drawdown period, the groundwater storage in the driving section is reduced by
438 an amount that approximately matches the reduction in the **resisting** section (Fig. 17(A)), so the
439 effect of buoyancy forces on slope stability is small. Moreover, because drawdown is slow,
440 groundwater gradients are also low, limiting the magnitude of destabilizing seepage forces. Thus, the
441 safety factor of the slope decreases from 1.031 to 1.018 with only a modest amount (Fig. 14(B)).

442 During the rapid drawdown phase, groundwater gradients are steeper and produce large,
443 destabilizing seepage forces on the slope (Fig. 18(A)). The sharp decline of slope stability (Fig.
444 17(B)) is consistent with the observed high **displacement** velocity during this phase. The slope
445 stability becomes least ($Fos=0.995$) as the reservoir declines to its lowest level of 145 m ASL, when
446 a maximum difference of 14 m is computed for groundwater levels in the slide mass (Fig. 17(B)).
447 Although the decreased buoyancy of the **resisting** section makes an offsetting contribution to slope
448 stability, its magnitude is small compared to that of destabilizing seepage forces.



449

450 **Fig. 17** Simulated groundwater tables over the period of generalized annual variation of reservoir
 451 water level in Stage 3. Gray shaded zone depicts the 145 to 175 m elevation interval. (A) slow
 452 drawdown phase; (B) rapid drawdown phase; (C) low level phase; (D) water level rising phase; (E)
 453 high water level phase



454

455 **Fig. 18** (A) Simulated pressure contours and flow vector at the end of rapid drawdown period (day
 456 165 in Fig. 17); (B) Simulated pressure contours and flow vector at the begin of high level period
 457 (day 303 in Fig. 17)

458

459

460

461

462

463

464

In the following three phases, representing the low water, rising and high water phases, the characteristics of the slope vary in a manner similar to those modeled in scenario 2. The stability of the landslide (see Fig. 14(B)) recovers gradually from 0.995 to 1.027 in the low water level phase, due to the dissipation of destabilizing seepage forces (Fig. 17(C)). Slope stability then increases rapidly as the reservoir level rises rapidly, when the seepage force reverses to become directed into the slope (Fig. 17(D), Fig. 18(B)). The slope obtains the highest stability with Fos value of 1.067 when the water level rises to the highest level 175 m ASL. Slope stability then decreases gradually as

465 that seepage force declines (Fig. 17(E)). All these results agree with the observed variations in
466 **displacement** velocity of the Shuping landslide (Sec. 4.2).

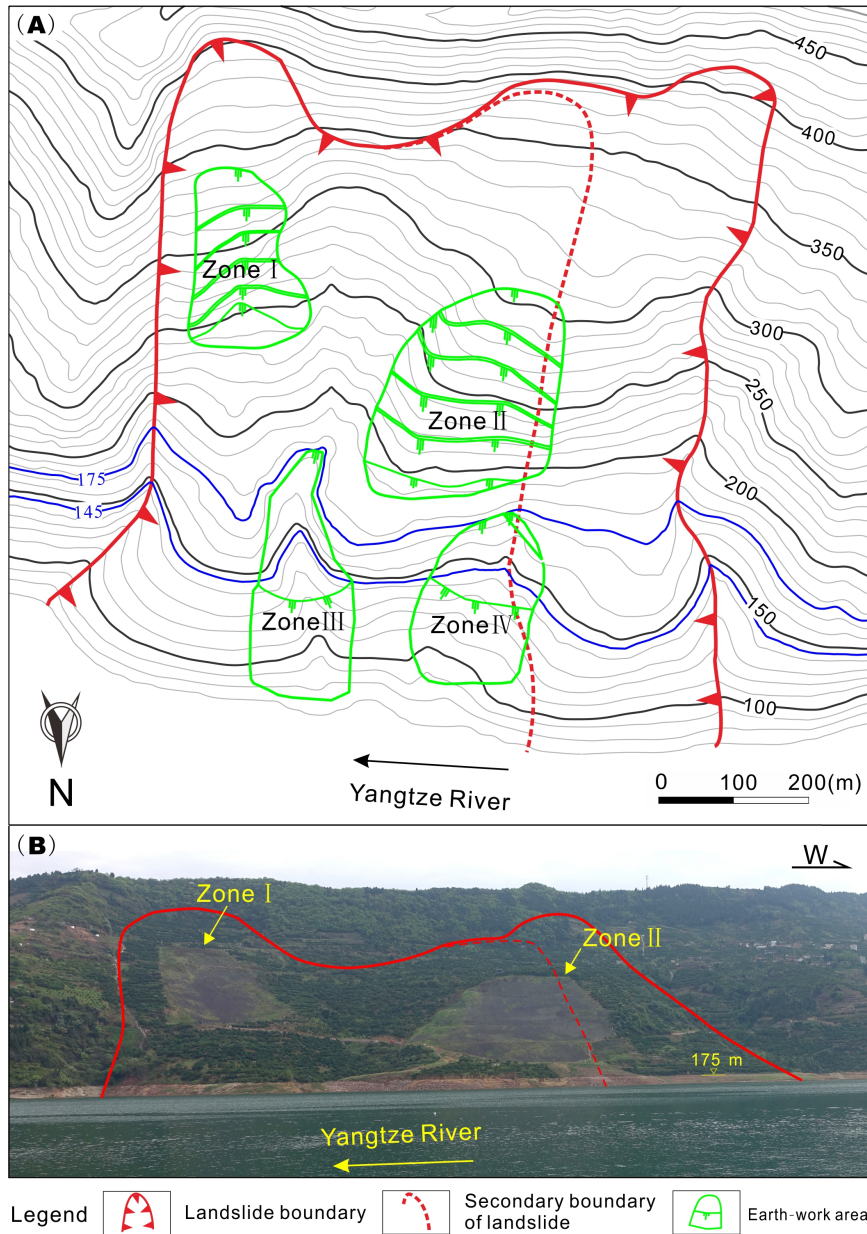
467 In summary, during periods of reservoir drawdown and rise, the seepage force plays a dominant
468 role in the stability of Shuping landslide, but being negative in drawdown period and positive in the
469 rising period. In contrast, buoyancy effects become increasingly important during periods of steady
470 reservoir levels, as seepage forces steadily decrease.

471 **6 Discussion**

472 This deformation of the Shuping landslide is a function of reservoir levels but probably also
473 depends on the hydraulic character of its constituent material. The lower part of the slide mass that is
474 subject to reservoir level fluctuation is mainly composed of dense silty soil with very low hydraulic
475 conductivity. During periods of rapid change in reservoir level, large differences in groundwater head
476 can be formed in such material, generating large seepage pressures that can either destabilize or
477 stabilize the mass, depending on whether the reservoir is rising or falling. On the other hand, low
478 permeability materials impede rainfall infiltration, rendering the landslide little influenced by rainfall.
479 Consequently, variations of the reservoir level and their attendant seepage forces dominate the
480 deformation of Shuping landslide.

481 Based on this observation and on the results of the driving-**resisting** model, two approaches are
482 recommended to control the deformation of huge reservoir landslides where the reinforcement
483 structures are difficult to construct. One method to improve stability is to transfer earth mass from
484 the driving section to the **resisting** section of the slide mass. The other is to use drains or pumps to
485 lower the water levels inside the slope, in order to reduce differences in groundwater head during

486 periods of reservoir drawdown. The first approach has in fact been adopted to enhance the stability of
487 Shuping landslide, which was conducted in September 2014 and completed in June 2015. Fig. 19(A)
488 presents the layout of the engineering treatment and Fig. 19(B) is the subsequent photo of Shuping
489 landslide. Zones I and II are the areas of load reduction, located in the driving section of the
490 slide mass. The earth mass of Zone I ($\sim 1.8 \times 10^5 \text{ m}^3$) and Zone II ($\sim 4.0 \times 10^5 \text{ m}^3$) were transferred
491 to Zones III and IV respectively, which are located in the resisting section that is mostly below
492 reservoir level in the photo (Fig. 18(B)). Monitoring data show that the displacement velocity was
493 significantly reduced to low values (about 4.1 mm/month in the main deformation area),
494 demonstrating the effectiveness of the engineering treatment. These approaches are more economical
495 and require a shorter construction period than many commonly-used remediation methods such as
496 the construction of stabilizing piles. Most importantly, these treatments are feasible for many other
497 large reservoir landslides.



498

499 **Fig. 19** Topography of Shuping landslide before (A) and after (B) engineering treatment, which
 500 involved the transfer of earth from Zones I and II to Zones III and IV.

501 The determination of the position of the boundary between driving and resisting sections is very
 502 complicated as it is related many factors. As the reservoir level varies, the stress of the landslide
 503 changes, which can affect the position of the boundary, and the position is dynamic. In this study, we
 504 proposed a static criterion to estimate the boundary position, that is, the boundary between the
 505 resisting and driving sections can be approximated as the position where the slope angle of the slide

506 surface equals the internal friction angle ϕ of the slide surface (section 2.2). This criterion was
507 effectively adopted to interpret the deformation process of the Shuping landslide. However, in the
508 situation that the sliding surface is irregular, a more rigorous method is required to determinate the
509 boundary postion.

510 **7 Conclusions**

511 A driving-**resisting** model is presented to elucidate the deformation mechanism of reservoir
512 landslides, as exemplified by Shuping landslide. The **displacement** velocity of Shuping landslide is
513 closely related to the variations in the level of the Three Gorges reservoir. Rainfall effects are limited
514 in comparison, perhaps due to the low hydraulic conductivity of the slide material. Rapid reservoir
515 drawdown produces large, destabilizing seepage forces in the slope of the slide mass, as evidenced
516 by large increases of its **displacement** velocity. In contrast, rising reservoir levels reverse the
517 direction of the seepage force, improving slope stability and decreasing the **displacement** velocity.
518 The buoyancy effect on the **resisting** section decreased the slope stability when the reservoir first rose
519 to 135 m ASL, but this effect has diminished as the reservoir has attained higher levels that buoy
520 both the driving and **resisting** sections.

521 Monitoring data, the driving-**resisting** model, and a successful engineering treatment suggest two
522 means to increase the stability of landslides in the TGR area. Recommended approaches are: 1)
523 transferring earth mass from the driving section to the **resisting** section; and 2) lowering the ground
524 water levels inside the slope by drains or by pumping during periods of reservoir drawdown. The
525 first approach was successfully applied to the Shuping landslide and could be used to treat many

526 other huge landslides in the Three Gorges Reservoir area.

527 **Data availability**

528 The study relied on the observation data from Department of Land and Resources of Hubei
529 Province, China.

530 **Competing interests**

531 The authors declare that they have no conflict of interest.

532 **Acknowledgements**

533 This work was supported by the National Key R&D Program of China (No. 2017YFC1501305);
534 the Fundamental Research Funds for the Central Universities, China University of Geosciences
535 (Wuhan) (No. CUGCJ1701); and the National Natural Science Foundation of China (Nos. 41630643,
536 41827808, 41502290).

537

538 **9 References**

- 539 1. Baum, R.L., Fleming, R.W.: Use of longitudinal strain in identifying driving and resisting
540 elements of landslides. *Geol. Soc. Am. Bull.* 103, 1121–1132, 1991
- 541 2. Casagli, N., Rinaldi, M., Gargini, A., and Curini, A.: Monitoring of pore water pressure and
542 stability of streambanks: results from an experimental site on the Sieve River, Italy, *Earth Surface
543 Processes and Landforms*, 24, 1095-1114, [https://doi.org/10.1002/\(SICI\)1096-9837\(199911\)24:
544 12<1095::AID-ESP37>3.0.CO;2-F](https://doi.org/10.1002/(SICI)1096-9837(199911)24:12<1095::AID-ESP37>3.0.CO;2-F), 1999.
- 545 3. Chang, S.B., Zhang, S.M. and Xiang B.: Engineering geology manual. China Architecture &
546 Building Press, Beijing, 2007 (in Chinese).
- 547 4. Cojean, R., and Cai, Y.J.: Analysis and modeling of slope stability in the Three-Gorges Dam
548 reservoir (China) -The case of Huangtupo landslide, *Journal of Mountain Science*, 8, 166-175,
549 <https://doi.org/10.1007/s11629-011-2100-0>, 2011.
- 550 5. Du, J., Yin, K., and Lacasse, S.: Displacement prediction in colluvial landslides, three Gorges
551 reservoir, China, *Landslides*, 10, 203-218, <https://doi.org/10.1007/s10346-012-0326-8>, 2013.
- 552 6. Dumperth, C., Rohn, J., Fler, A., and Xiang, W.: Local-scale assessment of the displacement
553 pattern of a densely populated landslide, utilizing finite element software and terrestrial radar
554 interferometry: a case study on Huangtupo landslide (PR China), *Environmental Earth Sciences*,
555 75, 880, <http://doi.10.1007/s12665-016-5475-y>, 2016.
- 556 7. Froude, M. J., and Petley, D. N.: Global fatal landslide occurrence from 2004 to 2016, *Natural
557 Hazards and Earth System Sciences*, 18, 2161-2181, <https://doi.org/10.5194/nhess-18-2161-2018>,
558 2018.

- 559 8. Guerriero, L., Coe, J.A., Revellino, P., Grelle, G., Pinto, F., and Guadagno, F.M.:
560 Influence of slip-surface geometry on earth-flow deformation, Montaguto earth flow, southern
561 Italy: *Geomorphology*, 219, 285-305, <http://dx.doi.org/10.1016/j.geomorph.2014.04.039>, 2014.
- 562 9. Handwerger, A.L., Roering, J., Schmidt, D.A., and Rempel, A.W.: Kinematics of earthflows in the
563 Northern California Coast Ranges using satellite interferometry, *Geomorphology*, 246, 321-333,
564 <https://doi.org/10.1016/j.geomorph.2015.06.003>, 2015.
- 565 10. Hu, X. W., Tang, H. M., and Liu, Y. R.: Physical model studies on stability of Zhaoshuling
566 landslide in area of Three Gorges Reservoir, *Chinese Journal of Rock Mechanics and Engineering*,
567 24, 2089-2095, 2005 (in Chinese).
- 568 11. Huang, B. L., Yin, Y. P., Wang, S. C., Tan, J., M., and Liu, G. N.: Analysis of the Tangjiaxi
569 landslide-generated waves in the Zhexi Reservoir, China, by a granular flow coupling model,
570 *Natural Hazards and Earth System Sciences*, 17, 657-670,
571 <https://doi.10.5194/nhess-17-657-2017>, 2017.
- 572 12. Huang, D., and Gu, D. M.: Influence of filling-drawdown cycles of the Three Gorges reservoir
573 on deformation and failure behaviors of anacinal rock slopes in the Wu Gorge, *Geomorphology*,
574 295, 489-506, <https://doi.org/10.1016/j.geomorph.2017.07.028>, 2017.
- 575 13. Huang, F. M., Huang, J. S., Jiang, S. H., and Zhou, C. B.: Landslide displacement prediction based
576 on multivariate chaotic model and extreme learning machine, *Engineering Geology*, 218, 173-186,
577 <https://doi.org/10.1016/j.enggeo.2017.01.016>, 2017.
- 578 14. Hubei Province Geological Environment Terminus: Survey report of Shuping landslide in Three
579 Gorges Reservoir area, Zigui, Hubei Province, China, 2013 (in Chinese).

- 580 15. Hutchinson, J.N.: An influence line approach to the stabilization of slopes by cuts and fills,
581 *Canadian Geotechnical Journal*, 21, 363-370, <https://doi.org/10.1139/t84-036>, 1984.
- 582 16. Iverson, R.M.: Unsteady, nonuniform landslide motion: 2. Linearized theory and the kinematics of
583 transient response, *Journal of Geology*, 94, 349-364, <https://doi.org/10.1086/629034>, 1986.
- 584 17. Jia, G. W., Zhan, T. L., Chen, Y. M., and Fredlund, D. G.: Performance of a large-scale slope
585 model subjected to rising and lowering water levels, *Engineering Geology*, 106, 92-103,
586 <https://doi.org/10.1016/j.enggeo.2009.03.003>, 2009.
- 587 18. Junfeng Z., Xiangyue M., and Erqian Z.: Testing study on landslide of layered slope induced by
588 fluctuation of water level, *Chinese Journal of Rock Mechanics and Engineering*, 23, 2676-2680,
589 2004 (in Chinese).
- 590 19. Lambe, T. W., and Whitman, R. V.: *Soil mechanics SI version*, John Wiley & Sons, 2008.
- 591 20. Lane, P. A., and Griffiths, D. V.: Assessment of stability of slopes under drawdown conditions,
592 *Journal of geotechnical and geoenvironmental engineering*, 126, 443-450,
593 [https://doi.org/10.1061/\(ASCE\)1090-0241\(2000\)126:5\(443\)](https://doi.org/10.1061/(ASCE)1090-0241(2000)126:5(443)), 2000.
- 594 21. Li, D., Yin, K., and Leo, C.: Analysis of Baishuihe landslide influenced by the effects of reservoir
595 water and rainfall, *Environmental Earth Sciences*, 60, 677-687,
596 <https://doi.org/10.1007/s12665-009-0206-2>, 2010.
- 597 22. Liao, H. J., Sheng, Q., Gao, S. H., and Xu, Z. P.: Influence of drawdown of reservoir water level
598 on landslide stability, *Chinese Journal of Rock Mechanics and Engineering*, 24, 3454-3458, 2005
599 (in Chinese).
- 600 23. Lu, S. Q., Yi, Q. L., Yi, W., Huang, H. F., and Zhang, G. D.: Analysis of deformation and failure

- 601 mechanism of Shuping landslide in Three Gorges reservoir area. *Rock and Soil Mechanics* 35(4),
602 1123-1130, 2014 (in Chinese).
- 603 24. Lu, T.: Study of Formation Mechanism and Later Trend Prediction of Fanjiaping Landslide and
604 Baishuihe Landslide, Dissertation, China Three Gorges University (in Chinese).
- 605 25. Ma, J. W., Tang, H. M., Hu, X. L., Bobet A., Zhang, M., Zhu, T. W., Song, Y. J., and Eldin M. A.
606 E.: Identification of causal factors for the Majiagou landslide using modern data mining methods,
607 *Landslides*, 14, 311-322, <https://doi.org/10.1007/s10346-016-0693-7>, 2017.,
- 608 26. McKean, J. and Roering, J.: Objective landslide detection and surface morphology mapping using
609 high-resolution airborne laser altimetry, *Geomorphology*, 57, 331-351,
610 [https://doi.org/10.1016/S0169-555X\(03\)00164-8](https://doi.org/10.1016/S0169-555X(03)00164-8), 2004.
- 611 27. Miao, F. S., Wu, Y. P., Li, L. W., Tang, H. M., and Li, Y. N.: Centrifuge model test on the
612 retrogressive landslide subjected to reservoir water level fluctuation, *Engineering geology*, 245:
613 169-179, <https://doi.org/10.1016/j.enggeo.2018.08.016>, 2018.
- 614 28. Paronuzzi, P., and Bolla, A.: The prehistoric Vajont rockslide: an updated geological model,
615 *Geomorphology*, 169, 165-191, <https://doi.org/10.1016/j.geomorph.2012.04.021>, 2012.
- 616 29. Prokešová, R., Kardoš, M., Tábor, P., Medvedová, A., Stacke, V., Chudy, F.: Kinematic
617 behaviour of a large earthflow defined by surface displacement monitoring, dem differencing, and
618 ERT imaging, *Geomorphology* 224, 86-101, <https://doi.org/10.1016/j.geomorph.2014.06.029>,
619 2014.
- 620 30. Qin, H. B.: The Mechanism of Landslide Influenced by Rainfall and Reservoir Water Level
621 Fluctuation and Renewed Criterion Research in Three-Gorges Reservoir, Dissertation, China

- 622 Three Gorges University, 2011(in Chinese).
- 623 31. Ren, F., Wu, X. L., and Zhang, K. X., and Niu, R. Q.: Application of wavelet analysis and a
624 particle swarm-optimized support vector machine to predict the displacement of the Shuping
625 landslide in the Three Gorges, China, *Environmental earth sciences*, 73, 4791-4804,
626 <https://doi.org/10.1007/s12665-014-3764-x>, 2015.
- 627 32. Rinaldi, M., and Casagli, N.: Stability of streambanks formed in partially saturated soils and
628 effects of negative pore water pressures: the Sieve River (Italy), *Geomorphology*, 26, 253-277,
629 <https://doi.org/10.1007/s12665-014-3764-x>, 1999.
- 630 33. Rinaldi, M., Casagli, N., Dapporto, S., and Gargini, A.: Monitoring and modelling of pore water
631 pressure changes and riverbank stability during flow events, *Earth Surface Processes and
632 Landforms*, 29, 237-254, <https://doi.org/10.1002/esp.1042>, 2004.
- 633 34. Song, W. P.: The unsaturated seepage and stability analysis on slopes at river banks with the case
634 of Xicheng landslides in Yunyang. Dissertation, Chengdu University of Technology, 2011(in
635 Chinese).
- 636 35. Song, K., Wang, F. W., Yi, Q. L., and Lu, S. Q.: Landslide deformation behavior influenced by
637 water level fluctuations of the Three Gorges Reservoir (China), *Engineering Geology*, 247, 58-68,
638 <https://doi.org/10.1016/j.enggeo.2018.10.020>, 2018.
- 639 36. Song, K., Yan, E. C., Zhang, G. D., Lu, S. Q., and Y, Q. L.: Effect of hydraulic properties of soil
640 and fluctuation velocity of reservoir water on landslide stability, *Environmental earth sciences*, 74,
641 5319-5329, <https://doi.org/10.1007/s12665-015-4541-1>, 2015.
- 642 37. Sultan, H.A., and Seed, H.B.: Stability of sloping core earth dams, *Journal of the Soil Mechanics*

- 643 **and Foundations Division, 93, 45-68, 1967.**
- 644 38. Tang, H. M., Li, C. D., Hu, X. L., Su, A. J., Wang, L. Q., Wu, Y. P., Criss, R. E., Xiong, C. R.,
645 and Li, Y. A.: Evolution characteristics of the Huangtupo landslide based on in situ tunneling and
646 monitoring, *Landslides*, 12, 511-521, <https://doi.org/10.1007/s10346-014-0500-2>, 2015.
- 647 39. Tang, H. M., Wasowski, J., and Juang, C. H.: Geohazards in the three Gorges Reservoir Area,
648 China - Lessons learned from decades of research, *Engineering Geology*, 261,
649 <https://doi.org/10.1016/j.enggeo.2019.105267>, 2019.
- 650 40. **Terzaghi, K., Peck, R. B., Mesri, G.: Soil mechanics in engineering practice, John Wiley & Sons,**
651 **1996.**
- 652 41. Wang, F.: Deformation prediction of Jiuxianping landslide in Yunyang Country based on
653 numerical simulation, Dissertation, Chengdu University of Technology, 2013 (in Chinese).
- 654 42. Wang, F., Zhang, Y., Wang, G., Peng, X., Huo, Z., Jin, W., and Zhu, C.: Deformation features of
655 Shuping landslide caused by water level changes in Three Gorges Reservoir area, China, *Chinese*
656 *Journal of Rock Mechanics and Engineering*, 26, 509-517, (in Chinese).
- 657 43. Wang, J. E., Xiang, W., and Lu, N.: Landsliding triggered by reservoir operation: a general
658 conceptual model with a case study at Three Gorges Reservoir, *Acta Geotechnica*, 9, 771-788,
659 <https://doi.org/10.1007/s11440-014-0315-2>, 2014.
- 660 44. Wang, H. L., and Xu, W. Y.: Stability of Liangshuijing landslide under variation water levels of
661 Three Gorges Reservoir, *European Journal of Environmental and Civil Engineering*, 17(sup1):
662 s158-s177, <https://doi.org/10.1080/19648189.2013.834592>, 2013.
- 663 45. Wen, T., Tang, H. M., Wang, Y. K., Lin, C. Y., and Xiong, C. R.: Landslide displacement

- 664 prediction using the GA-LSSVM model and time series analysis: a case study of Three Gorges
665 Reservoir, China, *Natural Hazards and Earth System Sciences*, 17, 2181-2198,
666 <https://doi.org/10.1002/esp.1042>, 2017.
- 667 46. Wu, Q., Tang, H. M., Ma, X. H., Wu, Y. P., Hu, X. L., Wang, L. Q., Criss, R. E., Yuan, Y., and Xu,
668 Y. J.: Identification of movement characteristics and causal factors of the Shuping landslide based
669 on monitored displacements, *Bulletin of Engineering Geology and the Environment*, 78,
670 2093-2106, <https://doi.org/10.1007/s10064-018-1237-2>, 2019.
- 671 47. Xiao, S. R., Liu, D. F., and Hu, Z. Y.: Study on geomechanical model of Qianjiangping landslide,
672 Three Gorges Reservoir, *Rock and Soil Mechanics*, 28, 1459-1464, 2007 (in Chinese).
- 673 48. Yin, Y., Huang, B., Wang, W., Wei, Y., Ma, X., Ma, F., and Zhao, C.: Reservoir-induced landslides
674 and risk control in Three Gorges Project on Yangtze River, China, *Journal of Rock Mechanics and*
675 *Geotechnical Engineering*, 8, 577-595, <https://doi.org/10.1016/j.jrmge.2016.08.001>, 2016.
- 676 49. Zou, Z., Yan, J., Tang, H., Wang, S., Xiong, C., Hu, X.: A shear constitutive model for describing
677 the full process of the deformation and failure of slip zone soil, *Engineering Geology*,
678 <https://doi.org/10.1016/j.enggeo.2020.105766>, 2020.